Summer 2015

Investigation of Electrical and Magneto Transport Properties of Reduced Graphene Oxide Thin Films

Ariful Haque

INVESTIGATION OF ELECTRICAL AND MAGNETO TRANSPORT PROPERTIES OF REDUCED GRAPHENE OXIDE THIN FILMS

A Masters Thesis

Presented to

The Graduate College of

Missouri State University

In Partial Fulfillment

Of the Requirements for the Degree

Master of Science, Materials Science

By

Ariful Haque

July 2015

INVESTIGATION OF ELECTRICAL AND MAGNETO TRANSPORT PROPERTIES OF REDUCED GRAPHENE OXIDE THIN FILMS

Physics, Astronomy and Materials Science

Missouri State University, July 2015

Master of Science

Ariful Haque

ABSTRACT

Large area uniform thin films of reduced graphene oxide (RGO) was synthesized by pulsed laser deposition (PLD) technique. A number of structural properties including the defect density, average size of sp^2 clusters, and degree of reduction were investigated by Raman spectroscopy and X-ray diffraction (XRD) analysis. The temperature dependent (5K - 350K) four terminal electrical transport property measurement confirms variable range hopping and thermally activated transport mechanism of the charge carriers at low (5K - 210K) and high temperature (210K - 350K) regions, respectively. The calculated localization length, density of states (DOS) near Fermi level (E_F), hopping energy, and Arrhenius energy gap provide significant information to explain excellent electrical properties in the RGO films. Hall mobility measurement confirms *p*-type characteristics of the thin films. The charge carrier Hall mobility can be engineered by tuning the growth parameters, and the measured maximum mobility was 1596 $cm^2V^{-1}s^{-1}$ in the optimum sample. The optimization of the improved electrical property is well supported by Raman spectroscopy. The magneto resistance (MR) effect in the thin films provides sufficient information to reinforce the obtained electrical property information. The maximum values of measured positive MR are 27% and 12% at low (25K) and room (300K) temperatures, respectively. The transport properties of RGO samples are dependent on a number of factors including the density of the defect states, size of the sp^2 clusters, degree of reduction, and the morphology of the thin film.

KEYWORDS: Graphene, Graphene Oxide, Variable Range Hopping, Raman Spectroscopy, Electrical Transport Property, and Magneto Resistance.

This abstract is approved as to form and content

_____

Kartik Ghosh, Ph.D.
Chairperson, Advisory Committee
Missouri State University

INVESTIGATION OF ELECTRICAL AND MAGNETO TRANSPORT PROPERTIES OF REDUCED GRAPHENE OXIDE THIN FILMS

By

Ariful Haque

A Masters Thesis
Submitted to the Graduate College
Of Missouri State University
In Partial Fulfillment of the Requirements
For the Degree of Master of Science, Materials Science

July 2015

Approved:

_____
Kartik Ghosh, PhD

_____
Robert A. Mayanovic, PhD

_____
Adam Wanekaya, PhD

_____
Julie Masterson, PhD, Dean, Graduate College

ACKNOWLEDGEMENTS

Foremost, I would like to thank my mentor and advisor *Dr. Kartik Ghosh* for his timely suggestions and guidance throughout the process of completing my Masters. Without his guidance, I would not be where I am today.

I am fortunate to have worked with an excellent thesis committee: *Dr. Kartik Ghosh, Dr. Robert A. Mayanovic and Dr. Adam Wanekaya*. Thank you all for agreeing to be a part of my thesis committee.

I would like to express my gratitude to my professors in my previous school *Dr. Mohammad Ali Chaudhury, Dr. Md. Quamrul Ahsan,* and *Dr. Saifur Rahman*. They carry in common a passion for their students, and a desire for their students to succeed.

I would like to thank my friends for all the support and encouragement. There are too many of you to mention but I would especially like to thank *Anagh Bhaumik, Mohammad F. N. Taufique, Priyanka Karnati,* and *Md. Abdullah-Al Mamun.* Thanks for always being up for a good laugh over the years. Many others have helped shape my views, research and took the time to comment on sections of this dissertation during its evolution. Thanks to all of you.

I am grateful to my parents for their constant support and they are always there for me when I need them. I am also thankful to my sister, and brother for cheering me up throughout the whole journey. Without the support of aforementioned people this research study would have been impossible. There is no way I can put down on paper how much you all mean to me, I thank you all.

TABLE OF CONTENTS

LIST OF TABLES

LIST OF FIGURES

CHAPTER 1: INTRODUCTION

1.1 Graphene

Graphene is an allotrope of tightly packed carbon atoms sitting in a thin layer of hexagonal honeycomb structure. The pure carbon atoms are sp^2 bonded with a bond length of 0.142 nm.[1] It is the thinnest compound scientists have ever discovered which is at one atom thick. These layers of graphene stack on the top of each other with an interlayer separation of 0.335 nm to form graphite.[1] Graphene is the lightest material with specific surface area of 2630 m^2g^{-1}.[2] It is also the strongest material (tensile stiffness of 1100 GPa and fracture strength of 125 GPa)[3], the best conductor of electricity (charge carrier mobility is more than 200,000 $cm^2V^{-1}s^{-1}$),[4] and the best conductor of heat at ambient condition (4.84 x 10^3 to 5.30 x 10^3 $Wm^{-1}K^{-1}$).[5] It has unique levels of light absorption at $\pi\alpha \approx 2.3\%$ of white light, and is also a potential candidate for the use in spin transport.[5]

By mass, carbon is the second most abundant element in the universe which makes it the chemical basis for all known life in the planet earth. Therefore, graphene technology could be an echo-friendly and a sustainable solution for an enormous number of applications, particularly in electronics and biotechnology

1.2 Electronic Properties of Graphene

The well-known electronic property of graphene is its' zero bandgap semimetal nature with both electrons and holes take part in charge transportation. The outer shell electrons in each carbon atom are equally likely to take part in chemical bonding,

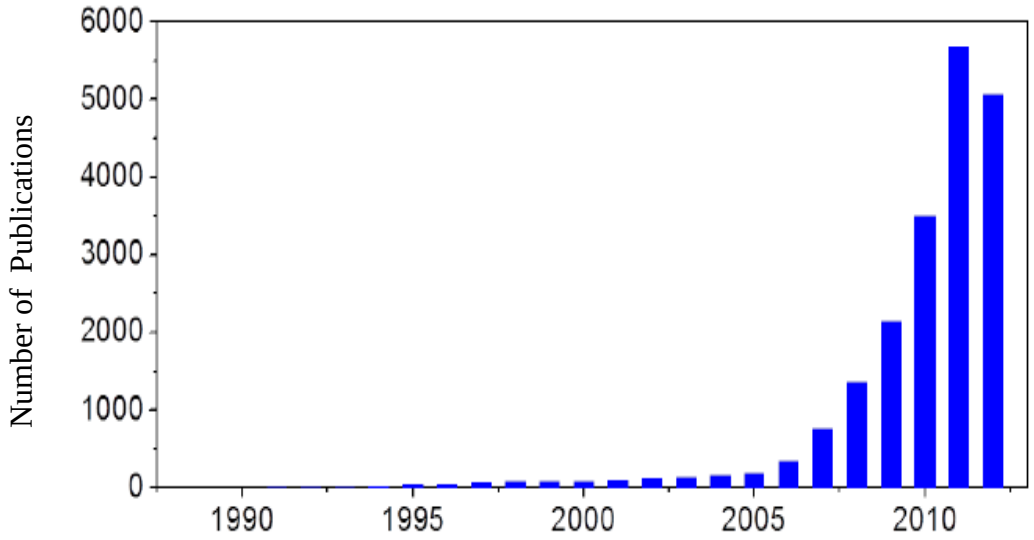

Figure 1.1: Number of publications on graphene and graphene oxide by year. (Constructed by searching for "graphene" in web of knowledge database)

but the sp^2 hybridized carbon atom in graphene is connected to three other carbon atoms in the 2D structure living behind 1 free electron. This free electron is available in the third dimension to take part in the electrical conduction process. Because of the suitable structure and band alignment of graphene, these free electrons possess high mobility under the electric field and are called π electrons. The π electrons are located above and below the graphene sheet. The overlap of the π orbitals helps enhance the strength of carbon-carbon bonds in graphene. Therefore, it is also important to note that the electronic properties of graphene are mainly governed by the bonding and anti-bonding (valance and conduction bands) of these π orbitals. Researchers have found that electrons and holes have zero effective mass at Dirac point in this 2D material. This is due to the energy momentum relation; the spectrum for excitations is linear in the range of low energy near the 6 individual corners of the Brillouin zone. These 6 corners of the Brillouin zone are known as the Dirac points and the conduction electrons and holes are known as Dirac fermions sometimes termed as graphinos. The electronic conductivity is

quite low because of the zero density of states (DOS) at the 6 Dirac points. Nevertheless, the Fermi level (E_F) can be tuned by changing the doping concentration with either electrons or holes to change the conductivity of a material. Though the theoretical limit of electronic mobility of graphene is 200,000 $cm^2V^{-1}s^{-1}$, the maximum experimental value reported till date is 15,000 $cm^2V^{-1}s^{-1}$.[1] The charge carriers are mainly limited by scattering of graphene's acoustic phonons. Due to the lack of mass, the free electrons in graphene behave similar to the photons in their mobility. These free electrons/ charge carriers can travel sub-micron distance without facing any scattering phenomena which is known as ballistic transportation. Nevertheless, there remains some other limiting factors such as the quality of graphene used for the test as well as the substrate on which the graphene is embedded. For example, on SiO_2 substrate the potential charge carrier mobility is limited to 40,000 $cm^2V^{-1}s^{-1}$.[1]

1.3 Graphene Oxide

Graphene oxide (GO) is a thin layer of carbon atoms produced by the oxidation of graphene using strong oxidizing agents, oxygenated functionalities. On both sides of the graphene layer, some carbon atoms are functionalized with different oxygen containing groups dominated by hydroxyl and epoxy groups and the edges are mainly dominated by carboxyl and lactol groups. The presence of the functional groups results not only the expansion of the interlayer distance but also makes the material hydrophilic. Mainly due to the presence of COOH groups and OH groups, GO can disperse and dissolve in basic solutions.

1.4 Properties of GO

One of the advantages of GO is its easy dispersibility in water and other organic solvents, as well as in different matrixes, due to the presence of the oxygen functionalities. This remains as a very important property when mixing the material with ceramic or polymer matrixes when trying to improve their electrical and mechanical properties.

Due to the disruption of sp^2 bonding networks, GO becomes an electrical insulator. In order to recover the electrical conductivity and other important properties of graphene, researchers usually follow different reduction routes. Functionalization and tuning the percentage of different functional groups in GO can change its fundamental properties. The resulting modified structure could then become more usable for a number of applications. The selection of the reduction process of GO mainly depends on the desired application. For example- to use GO in drug delivery application higher level of dispersibility of GO in organic solvent is required. Therefore, amines containing solvent is used for the organic covalent functionalization of graphene.

1.5 Structure of GO and RGO

The type and coverage of the oxygen containing functional groups on GO are dependent largely on the preparation processes. Mainly hydroxyls and epoxies are present on the basal planes of the GO structure. From a number of reports[6,7,8] it is found that a single layer of GO has a thickness of ~1 nm. The presence of oxygen-containing functional groups is mainly responsible for the increment in layer thickness. The interlayer separation in multilayer stack of dehydrated GO is ~0.6 nm.[1] The lateral

dimensions of a GO sample can vary from a few nm to hundreds of micro-meters.[9] Structurally, Lerf–Klinowski model is the widely accepted model of GO.[10,11] In this model, the representation of chemical arrangement of a single atomically thin layer of GO is also experimentally supported by several studies.[12]

Researchers have also proposed a complete model of GO structural where lactol rings consist of 5 and 6 members decorating the edges and esters of tertiary alcohols remain on the surface. [13] High-resolution transmission electron microscopy study on the defective nature of RGO confirms the presence of holes, Stone–Wales and other defects.[13] On the other hand, very few structural models have been proposed for RGO. Using first principles and molecular dynamics calculations, Bagri *et al.*[14] demonstrated that RGO is disordered. The creation of holes and discontinuous zones within the basal plane due to the evolution of CO and CO_2 in the reduction process are the main reasons for this type of disorder. In this study it was also shown that the residual oxygen (~7–8%) in highly reduced GO is an outcome of the formation of highly stable ether and carbonil groups. These functional groups cannot be removed without destroying the graphene basal plane. Although the strain is larger in GO layer, its atomic structure consists of the primary graphene plane.

GO is a two-dimensional network consisting of variable sp^2 and sp^3 concentrations. On the other hand graphene is a sheet of sp^2 carbon atoms. By controllable removal of desired oxygen groups the sp^2 fraction can effectively be engineered. This controllability can be effectively be used for tailoring the optical, electrical and/or chemical properties of GO. Both GO and RGO consist of non-stoichiometric and complex structure. Therefore the electronic as well as the optical

properties are dictated by a complicated interplay of size, processing technique, and most importantly the relative fraction of the sp^2 and sp^3 domains. The presence oxygen groups incorporate defects in GO and RGO structure which create chemically reactive sites. These sites allow these 2D materials to be split or cleaved into smaller sheets thereby generating nanosized GO/RGO or nanoribbons. These cleaved product usually show different properties from their original counterpart i.e. GO/RGO.

Though graphene is a highly stable thin sheet of carbon atoms with large charge carrier mobility, the incorporation of its valance band and conduction band at Fermi level make it a zero-gap semiconductor. Moreover, recent graphene/GO devices showed the presence of Schottky barriers raising further investigations of tuning the band gap by changing the degree of oxidation.[15] For opening up and controlling the band gap researchers followed different routes to decorate its basal plane with different oxygen containing functional groups such as epoxy (C-O-C), carbonyl(C=O), carboxyl (COOH), hydroxyl(C-OH) etc.[16] These oxygen containing functional groups convert graphene to GO which is a highly disordered insulating structure due to the abundance of sp^3 hybridized carbon clusters with respect to the ordered graphene structure. The sp^2 carbon sites comprises of conducting π - π^* states while the sp^3 matrix is completely insulating due to its large energy gap between the σ - σ^* states. In different magnetic property investigation studies on graphene based compounds, scientists have observed positive magneto resistance (MR), [17] negative MR,[18] and even a transition from positive to negative MR.[19] The origin of the magneto resistance effects was interpreted using weak localization, weak anti-localization, dominance of bi-polaronic mechanism, Lorentz force, scattering from localized magnetic moments created by impurities and vacancies,

and quantum interference model.[18,20,21,22] In some studies the effect of intense structural defects and disorderness have been correlated with the MR effect.[17, 23]

1.6 Objectives

The ratio between sp^2 and sp^3 fraction of carbon atoms in RGO can be controlled by governing the level of reduction which provides a dynamic feature to tune the band gap energy including the control over optical property. Therefore researchers followed several strategies such as chemical reduction,[24] thermal annealing reduction,[25] microwave irradiation[26] and laser irradiation reduction, [27] solvothermal reduction, [28] multistep reduction, [29] etc to convert the GO useable for semiconducting applications. The main goal of all the reduction mechanisms is to control the fraction of sp^2 and sp^3 hybridized carbon clusters. But in most of the reduction processes the structure of the GO turn into highly defective state because of the loss of C atoms from the basal plane. This loss of C atoms occurs due to the use of strong chemical reagent or immense localized heating effect. [30, 31] Moreover, few chemical reagents can only effectively remove the functional groups from the basal plane leaving the remaining edge moieties intact.[13] These disorder or defective sites along with the remaining sp^3 hybridized carbon sites hinder the charge carrier transport mechanism. As a result the charge carrier mobility becomes limited which affects its appeal to be used as a key material for next generation electronics. Furthermore the chemical route produces flakey RGO platelets whereas only large area continuous films can be used for potential electronic device applications. While integrating these flakes to fabricate large area thin film using different methods such as drop casting, dielectrophoresis, etc these flakes of RGO may cause discontinuity,

boundary defects, and overlapping which further deteriorate the electrical property.[32, 33] To retain the potential high charge carrier mobility of RGO with better conductivity my goal was to follow a completely novel route by fabricating large area thin film on Si/SiO_2 substrate using physical vapor deposition technique. To avoid the chemical reagent based reduction path which often consists of the use of toxic reducing compound such as N_2H_4 and $NaBH_4$ I wanted to use the pulsed laser deposition method.[13, 25] Because this nonconventional deposition process of RGO offers a number of tunable parameters to control the amount of sp^2/sp^3 carbon ratio and the degree of reduction. Although different structural, optical, vibrational, and transport studies were conducted to explain the level of reduction, charge carrier transport mechanism, band gap energy, and type of the charge carriers, I believe that with different growth mechanisms these properties might change. That is why to obtain detail information about this facile growth process my goal was to explore the structural, and optical properties of the as synthesized RGO films. I also wanted investigate the room and low temperature electrical transport properties of those RGO thin films to figure out the optimum parameters for the best quality film. These temperature dependent resistance measurement data would also help me to incorporate the Arrhenius and 2D VRH models of charge transportation in the thin film for explaining the transport mechanism. Furthermore, very few research studies have been conducted on the magnetic property of GO together with the study of electrical property. In this study I planned to investigate the electrical transport properties under the magnetic field to explore the magnetic properties of thus-synthesized RGO thin films. Finally, with the help of the structural, optical, magnetic, and surface morphology analysis my plan was to study the hidden factors because of the improved electrical property.

CHAPTER 2: VARIABLE RANGE HOPPING MODELS

2.1 Hopping Transport

Hopping is the transportation of electrons from a filled site to a vacant site by thermally effected tunneling process.[34] A disordered semiconductor with localized states shows finite value of conductivity for room temperature due to the process of electron hopping between localized states, and its resistivity tends to diverge as temperature is reduced. The dependence of resistance *R(T)* on temperature can be expressed as:

$$R(T) = R_0 \, e^{(\frac{T_0}{T})^p} \qquad 2.1$$

where R_0 is a prefactor , T_0 is the characteristic temperature and p is the characteristic exponent. The value of p distinguishes different hopping conduction mechanism. Miller and Abrahams[35] introduced "random resistor network" model to describe electron hopping between localized states. In this model, they considered a resistance R_{ij} between two localized sites i and j where hopping process takes place. This resistance explicitly depends on the distance between the sites, r_{ij} and on their energies by the following relation.[35]

$$R_{ij} = R_{ij}^0 \exp\left\{\frac{2r_{ij}}{a}\right\} \exp\{\frac{\epsilon_{ij}}{K_B T}\} \qquad 2.2$$

where, R_{ij}^0 is the typical resistance weakly dependent on the temperature and the surrounding, a is the bohr radius of the localization site, and the energy difference between i and j site, ϵ_{ij} is given by the following equation[36]-

$$\epsilon_{ij} = \frac{1}{2} \{|\epsilon_i - \epsilon_j| + |\epsilon_i - \mu| + |\epsilon_j - \mu|\} \qquad 2.3$$

where ϵ_i and ϵ_j are the energies at *i* and *j* sites respectively, and μ is the chemical potential. In presence of zero electric field, the rate of the hopping of electrons from *i* to *j* site is the same of that of from *j* to *i* site. For non-zero electric field these two rates are different and a constant current flow occurs between these two sites. This effective current along with the potential difference between *i* and *j* sites allow us to calculate the hopping probability of charge carriers between those two sites with absorption and emission of phonons. F2.1 is showing the whole phenomena of random resistor network model described above.

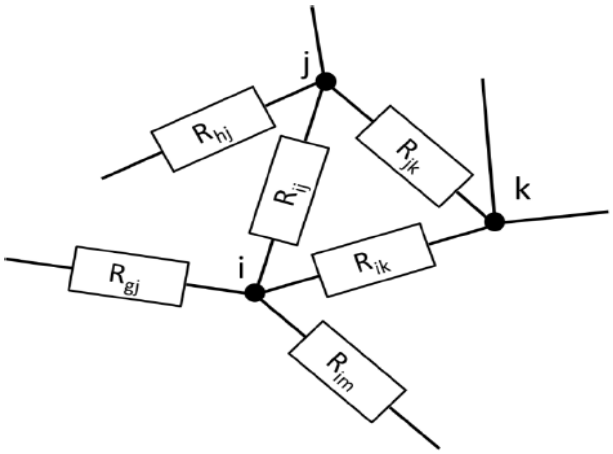

Figure 2.1: Random resistor network model.

2.2 Nearest Neighbor Hopping (NNH)

If two nearest neighbor localized states are separated by an energy E_0, then at temperature close to room temperature the electron can hop from one state to another with the assistance of thermally activated phonons. This concept is depicted in F2.2. In this case the hopping mechanism follows the following equation:

$$R(T) = R_0 \exp(\frac{E_0}{K_b T}) \qquad 2.4$$

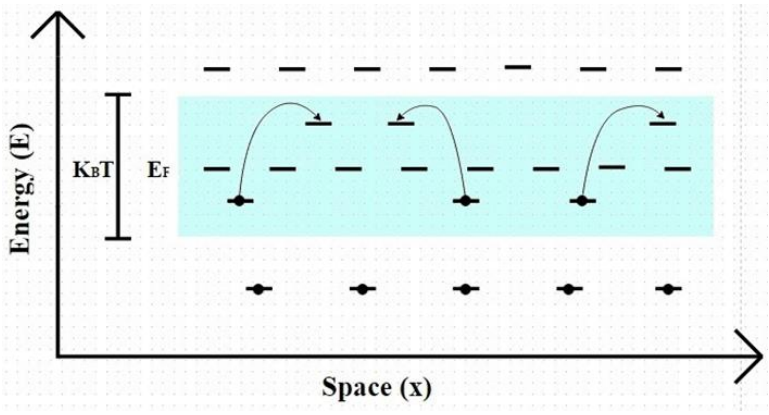

Figure 2.2: Nearest neighbor hopping conduction.

2.3 Mott VRH

In 1979, Mott and Davis (1979) observed that there exists a non-zero probability of the charge carriers at the Fermi energy (E_F) level to tunnel to a more distant localized state than those of the nearest neighbor states.

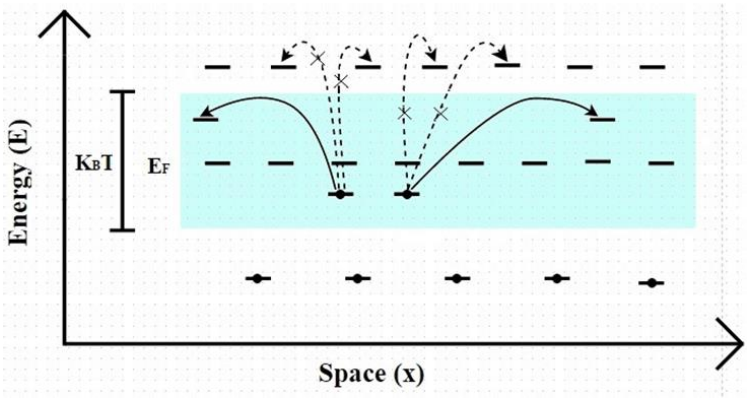

Figure 2.3: Mott variable range hopping conduction.

In doped semiconductors variable range hopping (VRH) conductivity can be imagined as a tunneling phenomenon which can be applied to the distribution of deeper states where charge carriers are not likely to attain sufficient energy to leave a trap.

Because the thermal energy (*KT*) is much smaller than the difference in energy between adjacent localized states. Therefore the elevation of these charge carriers to a local extended state is quite unlikely. But VRH conduction utilizes these deeper localized states at low temperatures. Nevertheless, these localized states contribute less to the overall conductivity of a semiconductor at high temperature regime but can dominate the charge carrier transport mechanism at low temperature region. The process can be explained as- in low temperature regime the localized wave function of the charge carrier has to sample over a larger volume to find out a suitable state whose energy is fine enough to be accessible. This concept is depicted in F2.3. So it is evident that the energy difference between the two localized states involved with electron transition in Mott VRH are separated by a larger distance than nearest neighbor distance but the energy difference E_{ij} is small which allows the hopping conduction at low temperature. The state lies within the Fermi level from E_F-E_0 to E_F+E_0. In Mott's argument the density of states at Fermi energy level, $n(E_F)$ is considered to be constant. The number of states in the energy gap between those two localization states becomes-

$$N(E_0) = n(E_F).2E_0 \qquad 2.5$$

If *d* is the dimensionality of the system, I can replace r_{ij} by $[N(E_0)]^{-1/d}$ in equation (2) and considering E_{ij}=E_0.

$$R_{ij} = R_0 \exp\left(\frac{2}{[(E_0)]^{\frac{1}{d}}\, a} + \frac{E_0}{k_b T}\right)$$

i.e.

$$R_{ij} = R_0 \exp\left(\frac{2}{[2n(E_F)E_0]^{\frac{1}{d}}\, a} + \frac{E_0}{k_b T}\right) \qquad 2.6$$

The maximum hopping probability condition is satisfied for the value of E_0 when the first derivative of the above equation with respect to E_0 equates to zero.

$$E_0 = exp(\frac{2k_bT}{[2n(E_F)]^{\frac{1}{d}} d\ a})^{\frac{d}{d+1}} \quad 2.7$$

Finally, substituting the above equation into equation 2.6 the Mott VRH relation can be obtained.

$$R(T) = R_0 \exp(\frac{T_0}{T})^{\frac{d}{d+1}} \quad 2.8$$

2.4 Efros-Shklovskii (ES) VRH

In 1975 Efros and Shklovskii revealed that coulomb interaction leads to a dip in the DOS at E_F at low temperature.[37] As a result when a charge carrier hops from one occupied state to another unoccupied state, it leaves a hole behind. The electrostatic energy between the electron and hole is not negligible in this case and the system must supply this energy to facilitate the hopping mechanism. Hence, the idea of constant DOS at E_F doesn't exist anymore in their study. Therefore, the required energy for the hopping of the charge carrier from one localized site with energy E_i to another with energy E_j is-

$$\Delta E = E_i - E_j - \frac{e^2}{\varepsilon r_{ij}} \quad 2.9$$

Where ε is the dielectric constant. Considering the vanishing nature of the DOS at E_F the temperature dependence of resistance can be described by the following equation-

$$R(T) = R_0\ e^{(\frac{T_0}{T})^{\frac{1}{2}}} \quad 2.10$$

Where T_0 is the characteristic temperature which can be expressed as the following.

$$T_0 = T_{ES} = \frac{2.8\ e^2}{4\ \pi\varepsilon\varepsilon_0 k_B \xi} \quad 2.11$$

The required source of energy for hopping conduction in ES VRH model can also be obtained from an applied electric field *(E).* At sufficiently high electric field the dependence of hopping process on temperature reduces strongly and the field dependence of resistance expression can be written as

$$R(E) \sim (\frac{E_0}{E})^{\frac{1}{2}} \qquad 2.12$$

Where $E_0 = \frac{2K_bT_{ES}}{e\,\xi}$.

The coulomb interaction in ES VRH is depicted in F2.4.

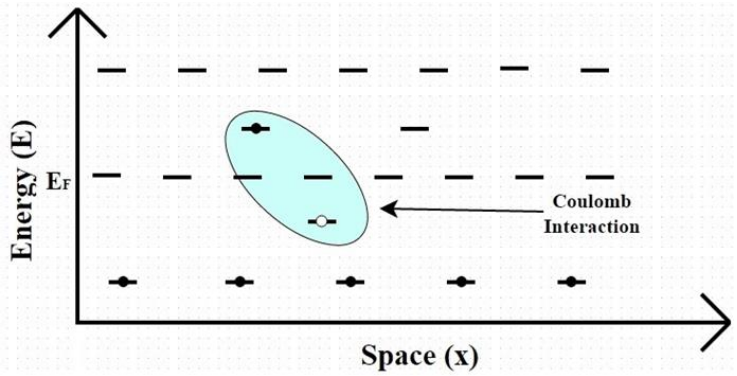

Figure 2.4: Coulomb interaction in ES variable range hopping conduction.

CHAPTER 3: DEVICE FABRICATION AND EXPERIMENTAL METHODS

3.1 Device Fabrication

RGO thin films were fabricated from a high purity graphite target using a pulsed laser deposition technique (Excel Instrument, PLD-STD-18). The source of the laser was Lambda Physik, COMPEX201 high energy UV KrF excimer laser. All the thin films were grown at an average laser energy of 325 mJ/pulse maintaining a frequency of 10Hz and a pulse duration of 20 ns. The Laser spot was focused on a 2.5 cm diameter high quality dense graphite target purchased from Kurt J. Leskar. The energy density of the focused laser spot was 2 Jcm^{-2}. In case of all the samples the separation between the target and the substrate was maintained at 3.5 cm. The substrate was 300 nm polished SiO_2 layer on n doped 400 μm *Si (*100) purchased from Siltronic Ag. On this substrate CVD grown graphene on Cu thin sheet was transferred using graphene transfer tape. First the adhesive layer of the graphene transfer tape was put on the graphene side of thin copper sheet using hand pressure. To etch out the Cu sheet, the graphene tape with Cu sheet was submerged into a solution of 0.5 M $FeCl_3$ solution for about 24 hours. Finally when the Cu sheet was completely etched out, the remaining carrier with graphene was washed several times using de ionized (DI) water. Afterward the carrier tape with the graphene was transferred onto the SiO_2(300nm)/Si substrate using moderate heating at 120 C. In this way the final transferred graphene is unlikely to be continuous and the resistance was found to be unmeasurable because of the discontinuity. The plume from the interaction between laser pulse and graphite target fills the discontinuous zones as well as controls the thickness of the thin film as a whole. Throughout the whole

deposition period a constant 700 C temperature was maintained. The chamber pressure was kept at 10^{-4}mbar which means there was enough oxygen, water, and Hydrogen molecules to interact with the sp^2 carbon moieties and partially convert them into sp^3 grade/clusters. After the deposition of the thin film a constant flow of forming gas (95% Ar and 5% H_2) was maintained throughout the cooling period. At this time the PLD chamber pressure was maintained at 10^{-3} mbar. The interaction between the H_2 in forming gas and the newly deposited thin film helps to reach further reduction level.

The seed layer of graphene helps grow films with better electronic properties which have been explored in the previous work done in our lab. The seed layer also boosts to reach to the desirable reduction level by improving the sp^2/sp^3 ratio tremendously. The dimension of all the fabricated RGO thin films are 5mm x 5mm. View representative of a representative film along with 4 contacts at 4 corners is shown in F3.1.

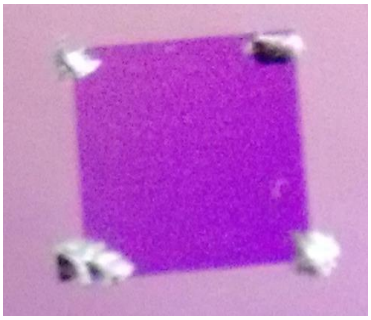

Figure 3.1: A representative RGO thin film sample with 4 contacts at the corners.

3.2 Pulsed Laser Deposition

Pulsed Laser Deposition (PLD) is a versatile and powerful technique to grow thin films and multilayers of complex materials. It consists of a vacuum chamber inside which a target holder and a substrate holder are placed. The energy source is a pulsed laser

source located outside the chamber. So the thin film can be grown in high vacuum and under ambient gas environment. The high power laser is directed towards the target using a set of optical components to focus and raster the beam over the target. The laser beam interacts with the target to vaporize materials and grow the thin film. Using this technique a stoichiometry transfer between the target and substrate takes place which allows the deposition of different types of materials such as oxides, carbides, nitrides, semiconductors, high-temperature superconductors and even metals.[38]

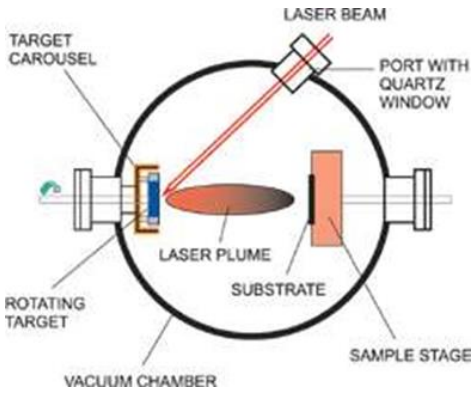

Figure 3.2: Schematic of pulsed laser deposition technique.

The pulsed nature of the PLD process even allows preparing complex polymer-metal compounds and multilayers as well as polymers and fullerenes. The preparation in inert gas or any other advantageous gas atmosphere makes it even possible to tune important film properties such as stress, texture, reflectivity, magnetic properties etc. by varying the kinetic energy of the deposited particles. That's why PLD is an alternative deposition technique for the growth of high-quality thin films.

3.3 Raman Spectroscopy

Raman spectroscopy is a non-destructive characterization technique comprises of the spectral measurements which provides information about molecular vibrations to identify and quantify different types of samples. This technique is also used to extract other important information of a material -such as- phase, composition, chemical bonding, crystal structure, chemical environment and to identify the number of layers of a 2 dimensional materials. In this technique a monochromatic source of light, usually a laser source is used to illuminate a sample. The oncoming monochromatic light can be considered as the oscillating electromagnetic field with electrical part E. Under this electric field the molecular polarizability α is determined to find out the Raman effect. Hence the resulting induced electric dipole moment, $P = \alpha E$ causes a perturbation in the molecule. In this way a periodic deformation is generated in the sample which causes the molecule to vibrate with its characteristic frequency υ_m. The sample absorb a fraction of the oncoming photon and reemits them. In comparison with the oncoming monochromatic frequency, the frequency of the reemitted photons shifts up, down or remains the same. If a molecule of a sample does not possesses any Raman active mode and absorbs a photon with frequency υ_0, it will return back to its original vibrational state by emitting the original frequency, υ_0. This type of scattering is called elastic Rayleigh scattering. On the other hand, if a Raman active molecule absorbs light with frequency υ_0, a part of the energy of the photon is transmitted to the Raman active mode with the characteristic frequency υ_m. As a result, the resulting frequency of the scattered photon is reduced to $\upsilon_0 - \upsilon_m$ which is called Stokes frequency and the whole phenomenon is known as stokes scattering.[39]

On the other hand, there is another type of scattering which is known as anti-stokes Raman scattering. At the time of interaction with photon with frequency, υ_0 if the Raman active molecule already exists in the excited vibrational state, the excessive photon energy is released by the excited molecule. Hence, the resulting frequency of the scattered light rises up to $\upsilon_0 + \upsilon_m$. This frequency is known as Anti-Stokes frequency or sometimes just 'anti-stokes'. In the photon interaction process about 99.99999% of the scattered photons undergoes elastic scattering which is not useful to receive the desirable characteristic information about a sample. Only about 10^{-5}% of the scattered photons are shifted in energy from the original frequency. However the stokes band is usually more intense than that of anti-stokes. Plotting the shifted light intensity versus the frequency provides the characteristic Raman peaks of the sample which is known as the Raman spectrum.

In F3.3 the difference between the incident photon energy and scattered photon energy is represented by the arrows with different heights. Numerically, the Raman shift $\bar{\upsilon}$ is the energy difference between the initial and final vibrational levels in the unit of wave numbers (cm^{-1}), is calculated using equation 3.1 where $\boldsymbol{\lambda}_{\text{incident}}$ is the wavelength of the incident photon and $\boldsymbol{\lambda}_{\text{scattered}}$ is the wavelength of the scattered photon.

$$\bar{\upsilon} = \frac{1}{\lambda_{incident}} - \frac{1}{\lambda_{scattered}} \qquad 3.1$$

A proper lens and optical filter setup is essential to obtain optimal data in Raman measurement. In our experiment I used an ILYMPUS MPlan N 50X/0.75 objective lens through which the green laser was focused on the sample. A band pass filter (BPF 532) was used to eliminate the unwanted radiations. I also used an edge filter (EDGE 532) to

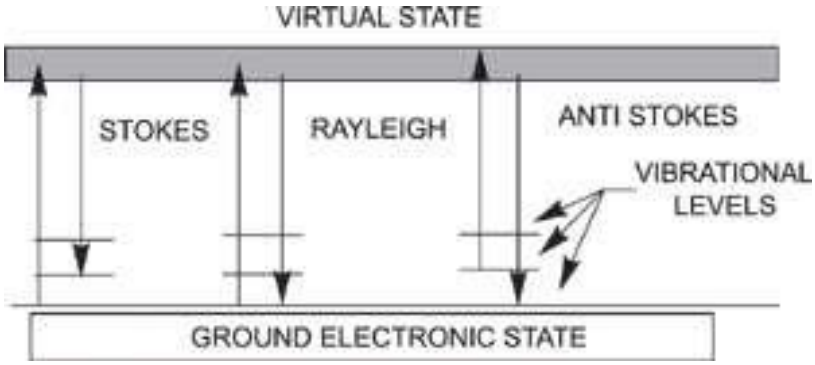

Figure 3.3: Electronic and virtual states along with vibrational levels in Raman spectroscopy.

block the frequencies coming from Rayleigh scattering. Before the measurement I calibrated the machine using a standard Si sample. To obtain the molecular vibrational spectroscopic information I have characterized all the RGO samples by Horiba Labram Raman-PL instrument. I used a green laser source of 532.06 nm wavelength (frequency doubled Nd:YAG) as an excitation source. The measured spot size was approximately 2.5 μm in diameter on the RGO thin film. Before performing the Raman characterization I confirmed that the intensity of laser source does not damage the sample. For all the measurements I used 15 seconds exposure time and 20 accumulation cycles. Over a substantial period of time I performed Raman measurement on transferred graphene on Si/SiO_2 substrate. This measurement showed the common spectra of transferred graphene where the position of the *D* band and *G* band were found at 1580 cm^{-1} and 2700 cm^{-1}, respectively.

3.4 X-Ray Diffraction

X-ray diffraction also known as XRD is a non-destructive analytic technique for identification and quantitative determination of different types of crystalline forms

sometimes termed as ‘phases’. The identification is performed by comparing the X-ray diffraction pattern with standard data.

Crystalline samples consist of parallel rows of atoms separated by a ‘unique’ distance. Diffraction occurs when the radiation enters a crystalline substrate and is scattered. The intensity of the pattern and the angle of diffraction depend on the orientation of crystal lattice with radiation.

XRD is mainly based on the constructive interference of monochromatic X-rays and a crystalline sample. The X-ray is generated by a cathode ray tube. This X-ray is filtered to produce monochromatic radiation, collimated to concentrate, and directed towards the sample. The interaction between the X-ray and sample produces constructive interference when the conditions match to Bragg’s Law. This law relates the lattice spacing in the crystal sample, wavelength of the X-ray radiation and the angle of diffraction. The sample is scanned through a range of 2θ angles in all possible diffractions. The diffracted X-ray intensity was processed and counted. When Bragg’s condition is satisfied, the number of counts rises and the XRD pattern gives a peak. Conversion of the diffraction peaks to *d*-spacing helps to identify the crystal structure. Because each crystalline material has a unique set of d-spacing.[40]

The XRD is typically used to measure the average spacing between the layers or rows of atoms, to determine the orientation of a single, crystal or grain, to find the crystal structure of an unknown material, and also to measure the size, shape and internal stress in thin film samples. To explore the structural information, I characterized the RGO thin films by Bruker, D8 Discover X-ray diffractometer using Cu Kα emission with λ = 1.5418 Å. The operating current and voltage was maintained at 40mA and 40 kV,

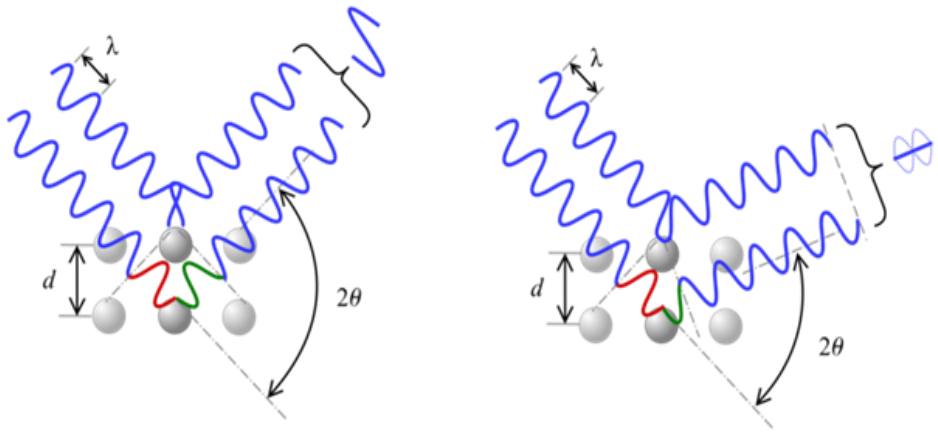

Figure 3.4: Illustration of Bragg's law. Depending on the angle the interference can either be constructive (left) or destructive (right). Figure from Wikipedia, contributed by Christophe Dang Ngoc Chan (2011).

respectively. The operated scan speed was 0.02^0 per degree and the step size was 6 throughout the whole run over the 2θ range 6^0 to 30^0.

3.5 SQUID Magnetometer

A superconducting quantum interference device (SQUID) is a mechanism used to measure extremely weak signals, even as subtle as a change in the electromagnetic energy field of the human body. According to John Clarke, one of the contributors to develop the concept of SQUID, this is the most sensitive measurement device made by the scientists. A device called a Josephson junction is used in SQUID, and can measure magnetic flux on the order of 1 flux quantum. I can visualize a flux quantum as the earth's magnetic field (5E-4 Tesla) passing through a single human red blood cell of diameter about 7 microns. It can measure extremely minute change in magnetic field up to 10E-32 Jules per second. A Josephson junction is made up of two superconductors, separated by an insulating layer.[41]

The insulating layer is so thin that electron can pass through the layer. A SQUID consists of tiny loops of superconductors employing Josephson junctions to achieve superposition: each electron moves simultaneously in both directions. As the current can move in two opposite directions simultaneously, the electrons have the ability to perform as qubits. Because of the ultra-sensitive nature, in this modern age SQUID is used for a variety of testing purposes in the field of engineering, medical, bio-medical and geological equipment.

The Quantum Design MPMS 5XL Superconducting Quantum Interference Device Magnetometer is situated in PAMS department to monitor any tiny change in magnetic flux to investigate the magnetic properties of any sample. Data can be collected over a wide range of field (-50000 Oe to +50000 Oe) and in the temperature range between 1.7K to 350K. The maximum sensitivity of this instrument is up to 10^{-9} emu. In our experiment I used a slow and steady temperature ramp and sent a constant current using the current source. Additionally, I measured and collected the voltage data as soon as the temperature reaches to the desired values in the four terminal measurement set up. The SQUID system provided us the facility to perform the transport experiments under a range of magnetic field up to 5T. The experimental technique along with the software I used will be discussed in details in chapter 4.

3.6 Hall Measurement

Hall effect is the development of a transverse electric potential in a solid material perpendicular to both an electric current flowing along the material and an external magnetic field applied in a direction perpendicular to the current flow. In physics and

engineering, Hall measurement is a very important tool to characterize any metal or semiconductor to determine the Hall mobility in the material, the charge carrier density and the type of the charge carriers in the given sample. In F3.5 the schematic diagram of the Hall measurement process is depicted. A rectangular conductor of width *w* and thickness *t* is placed in XY plane. Using a constant current generator (CCG), a constant current flow of density J_x is being flown in the X-direction. The applied magnetic field is along opposite to the Z axis. Therefore the Lorentz force, $F_m = q\ (v \times B)$, moves the charge carriers towards y-direction and results in an accumulation of the charge carriers at the top edge of the sample. Hence a transverse electric field, E_y is developed which is commonly known as Hall voltage V_H and the effect is called the Hall effect.[42]

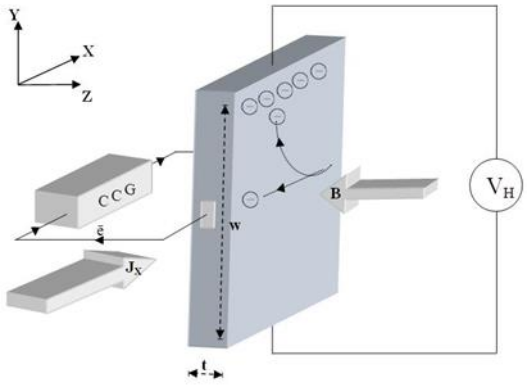

Figure 3.5: Schematic representation of Hall measurement in a sample.

The sign of V_H is important which helps to determine the type of charge carriers in the sample. If the V_H is negative which is very common in case of metals, the major charge carriers contribute to the conduction process is said to be electrons. On the other hand, if the V_H is positive, the major charge carriers are called hole. The Hall voltage that

develops while characterizing a sample is proportional to the applied current flow, the applied magnetic field, and inversely proportional to the carrier concentration and the thickness of the material in the direction of the applied magnetic field. Nevertheless, different materials possess different intrinsic properties, therefore they develop different Hall voltages under the same conditions i.e. size of the sample, flow of electric current, and applied magnetic field. In our measurement setup I synchronized the measurement tools in such a way that the voltage data were collected as soon as the magnetic field reached to the desired values while maintaining a constant current through the sample. The calculation of the charge carrier mobility and the type of electric charge in the RGO samples are described in the results and discussion section.

3.7 Electrical Transport Properties

All the electrical measurements were carried out using four point measurement setup which helps to avoid any possible effect from Schottky junction. The room temperature Hall measurement was done using Keithley 220 programmable current source, Keithley 182 sensitive digital voltmeter and magnetic coil powered by Power Ten P 63/66 Series high power analog dc supply programmed and run by derived by NI LabVIEW 2011 (National instrument). The temperature dependent transport measurement was performed by a system that uses the same current source and voltmeter. The sample was placed inside the Quantum Design superconducting quantum interference device magnetometer chamber. This system facilitates to maintain a constant rate of the increment of temperature and also provides an inert environment throughout the whole experiment. The temperature control, resistance measurement and the data

acquisition were done using an Electronic Data Capture (*EDC)* software at zero field and 5T field subsequently.

CHAPTER 4: RESULTS AND DISCUSSIONS

4.1 Raman Spectroscopy

F4.1 represents experimental and fitted Raman spectra of RGO thin films deposited by pulse laser deposition technique. From the fitted Raman spectra I observed that PLD grown RGO samples have all the characteristics peaks of GO in between 1000 cm^{-1} to 3000 cm^{-1}. The peak around 1585 cm^{-1} is the characteristic peak for sp^2 hybridized C-C bonds in graphene known as the *G* peak.[43] The peak around 1350 cm^{-1} is known as the *D* peak and it is activated when defects participate in the event of double resonance Raman scattering near K point of Brillouin zone [44]. The second order overtone of *D* peak around 2700 cm^{-1} is known as *2D* peak.[45] Scientists have found that *D* peak intensity is directly related to the defects on the structure. With increasing number of defects on the GO structure the intensity of *D* peak increases while that of 2D peak decreases.[58] The peak around 2950 cm^{-1} is a combination band of *D* peak and *G* peak and known as *D*+*G* peak. The *D*+*G* peak also depends on the defect concentration.[63] Researchers have found that the downshift of the *G* band position from 1600 cm^{-1} is an indication of p-type charge carrier in graphene based material.[57] This type of downshift in *G* band also indicates the recovery of sp^2 clusters of the GO structure.[40] In our case the *G* band position for all the samples lie in between 1590 cm^{-1} to 1596 cm^{-1}. This confirms the presence of *p* type charge carrier mobility and graphitization of the GO structure.

The I_D/I_G ratio has been used to calculate the average size of the sp^2 clusters of RGO structures by using the following formula.[46]

$$L_D^2(nm^2) = (1.8 * 10^{-9})\, \lambda_L^4\, (\frac{I_D}{I_G})^{-1} \qquad 4.1$$

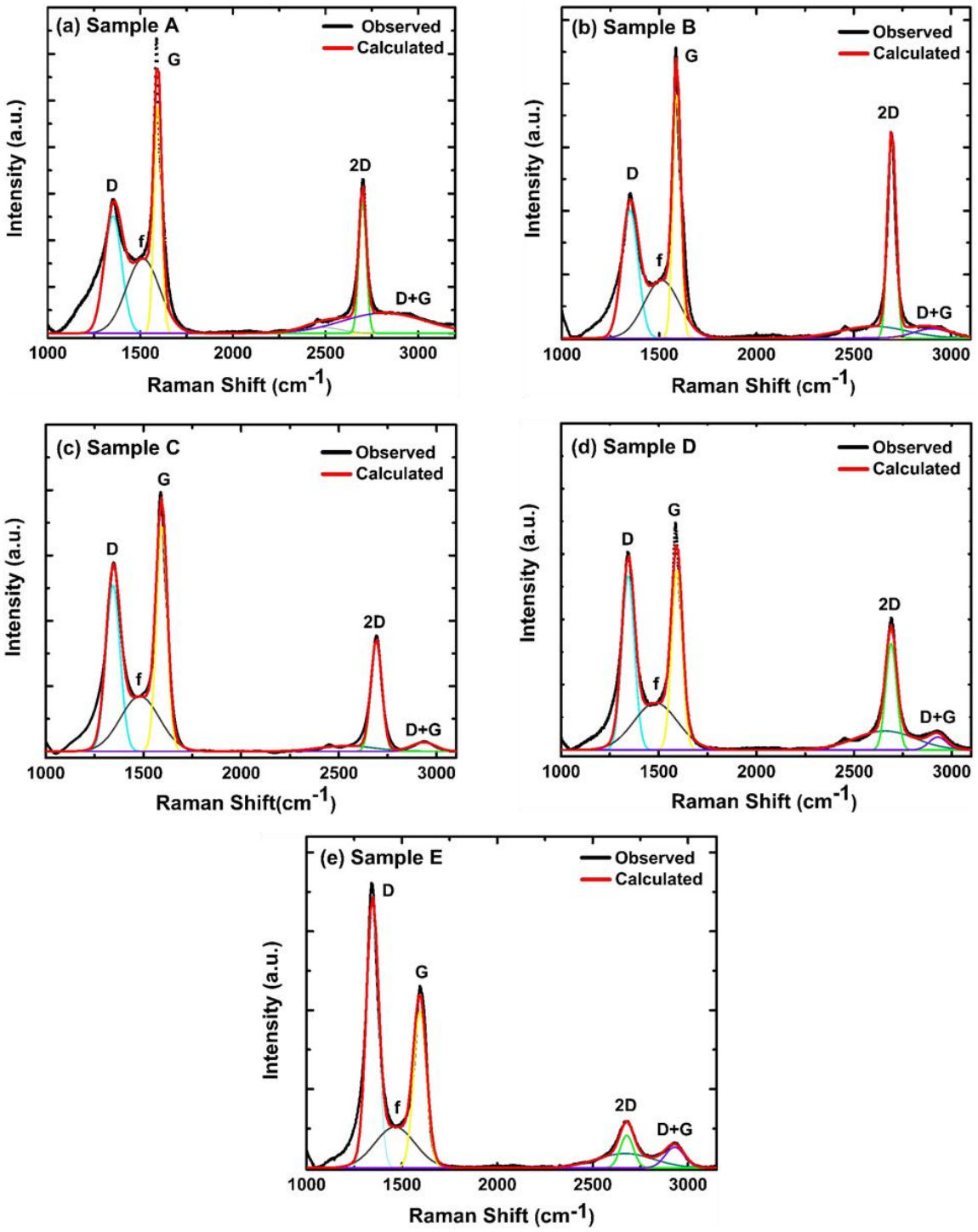

Figure 4.1: Raman spectra of the RGO thin film samples synthesized by PLD technique, (a) Sample A, (b) sample B, (c) sample C, (d) sample D, and (e) sample E.

Where L_D is the average size of the sp^2 domain and λ is the wavelength in nm (532 nm) of

the laser excitation. I have calculated the defect density n_D (cm^{-2}) in the 2D system by using the following formula.[57]

$$n_D\ (cm^{-2}) = \left(\frac{1.8*10^{22}}{\lambda_L^4}\right)\left(\frac{I_D}{I_G}\right) \qquad 4.2$$

Calculated value of the average size of the sp^2 domain, defect density of the GO structures, and peak intensity ratios are shown in T 4.1.

Table 4.1 Peak intensity ratios, sp^2 domain size, and density of the defect states calculated from fitted Raman spectroscopy data.

Sample	Number of Shots	I_D/I_G	I_{2D}/I_{D+G}	L_D (nm)	n_D (cm^{-2})
A	300	0.40	6.42	18.98	$8.98*10^{10}$
B	2000	0.52	21.6	16.65	$1.16*10^{11}$
C	5000	0.59	10.77	15.63	$1.32*10^{11}$
D	10000	0.79	9.03	13.50	$1.77*10^{11}$
E	20000	1.31	2.00	10.49	$2.94*10^{11}$

By conducting the thermal and gaseous reduction the structure of RGO approaches the graphene structure. As a result, the amount of disorder is less on the RGO structure and is justified by the decrease in the ratio between *D* and *G* band peak intensity, I_D/I_G.[47] The more it approaches to graphene, more the charge carrier mobility is expected in the sample. So I can predict that the samples with less I_D/I_G ratio could provide better charge carrier mobility.

Researchers have found significant amount of *2D* peak intensity in thermally reduced GO.[48] Due to the reduction a recovery of sp^2 clusters occurs and a dramatic

increase in the I_{2D}/I_{D+G} ratio takes place. Therefore I_{2D}/I_{D+G} ratio is an indicator for newly formed sp^2 clusters due to thermal reduction.[63] Higher value of I_{2D}/I_{D+G} signifies the larger charge carrier mobility as newly formed sp^2 cluster will provide the percolation path to the electrons. Overall the fitting information of Raman spectroscopy ascertain that all the PLD grown RGO samples have subsequent amount of graphitization which may help attain better charge carrier mobility.

4.2 X-Ray Diffraction

F4.2 represents the XRD pattern of a representative RGO thin film having the maximum hall mobility which explains the crystallinity of the film. The curve fitting for the XRD pattern has been done by using Origin Pro 8.1 software with the help of Gaussian-Lorentzian peak profile analysis.

The corresponding 2θ value for GO in the RGO sample is 12.2^0 which coincides with the previous results in which GO was synthesized by chemical process.[49, 50] GO has the largest interlayer (5Å - 9Å) distance because of the presence of intercalated water molecules and functional groups.[7] The calculated interlayer distance for GO is 7.24 Å. Presence of RGO is also evident from the XRD pattern, which may be due to the deposition of thin films at high temperature (700^0C). The 2θ value for RGO is 15.8^0 and corresponding interlayer distance (5.6 Å) has been decreased, due to the vaporization of water molecules present between the GO layers.[51] The crystallite size has been calculated using the Debye Scherer[52] formula and strain correction was used to calculate the FWHM (full width at half maximum) for the GO (36.38 Å) and RGO (18.14 Å) peaks.[53] Ju et al.[54] calculated the number of layers with the help of Debye Scherer formula, and the

corresponding values in our RGO thin film sample are found to be 5 and 3 in GO and RGO, respectively.

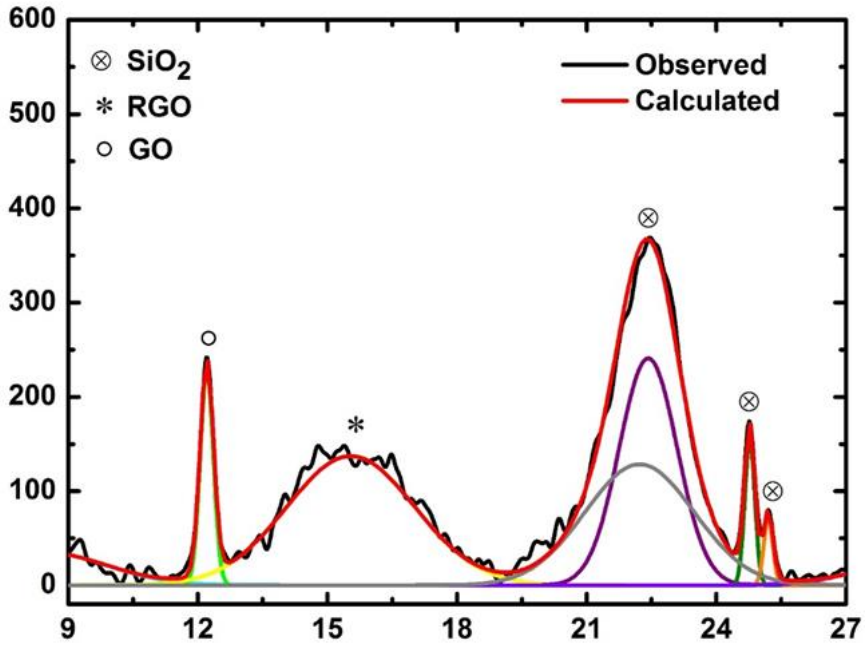

Figure 4.2 XRD pattern of RGO thin film.

4.3 Electrical Transport Mechanism

Hall measurement is an effective technique to investigate the electrical transport properties in graphene based materials conducted in different research studies.[55,56,57] F4.3 shows the Hall measurement plots for the RGO thin film samples fabricated on Si/SiO_2 substrate. The underlying semiconductor properties such as the Hall mobility μ, and charge carrier density n were calculated. The values of μ and n were calculated using the following equations.[55]

$$n = \frac{1}{R_H e} \tag{4.3}$$

$$\mu = \frac{1}{e\rho_s n} \tag{4.4}$$

Where the Hall constant R_H is the slope of the Hall resistance as a function of the applied magnetic field (B), ρ_s is the sheet resistance, and e is the fundamental charge of an electron. From the measured values it is evident that, with increasing the number of shots the charge carrier Hall mobility increases initially and for 5000 shots the mobility reaches to the maximum value. Thereafter the mobility starts decreasing at a slower rate with increasing the number of shots. From the plot of voltage as a function of magnetic field (B) in F4.3 it is also obvious that holes play the major role in charge carrier transport mechanism. The calculated value of the room temperature charge carrier concentration is in-between 1.84 x 10^{12} cm^{-2} to 1.26 x 10^{13} cm^{-2} which indicates high level of doping.[71] This doping might take place because of the presence of different functional groups in the RGO thin films. To comprehend the charge carrier transport process I performed the *R vs T* measurement.

Four probe electrical measurements were performed for all the RGO thin film samples. To study the conduction mechanism, the temperature dependent resistance measurements were carried out in a wide range of temperature (5K<T<350K). F4.5 shows the overall temperature dependent resistance data of the RGO samples at zero field and 5T. With decreasing temperature the trend of nonlinear increment in the resistance is consistent with many other semiconducting 2D systems.[58, 59] The essence of the resistance dependence on temperature can be split into two distinct regions. At high temperature regime, the resistance of the RGO thin films increases slowly with decreasing temperature. On the other hand at the low temperature regime the increment of the resistance was faster with the same rate of temperature decrement.

At the high temperature region the resistivity vs temperature curve correlates best

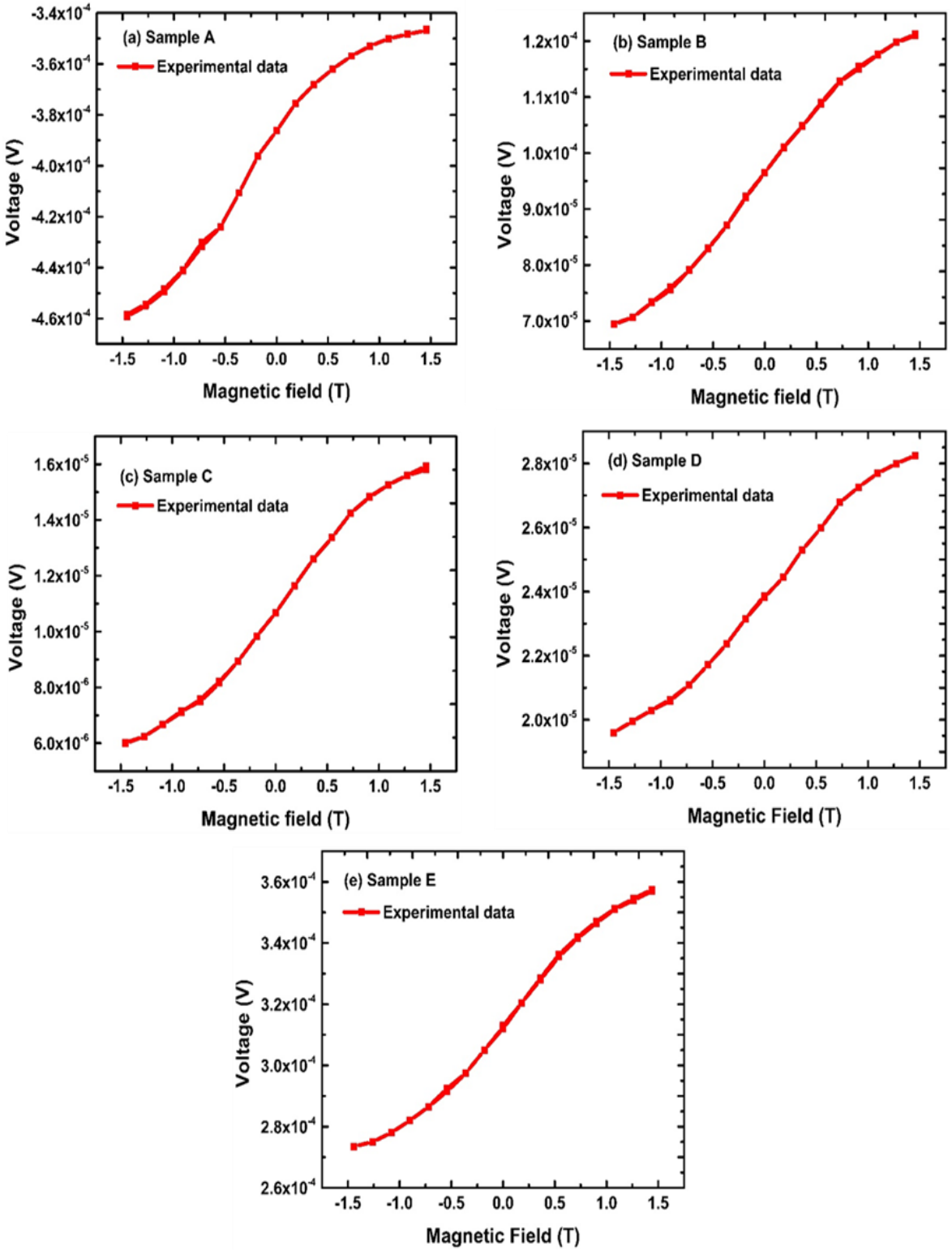

Figure 4.3: Hall measurement of (a) sample A, (b) sample B, (c) sample C, (d) sample D, and (e) sample E.

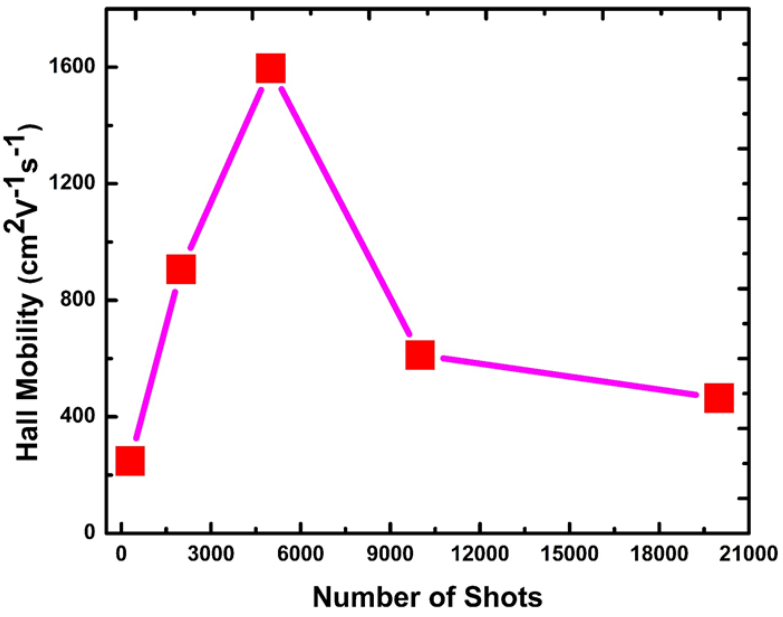

Figure 4.4: Hall mobility with respect to the number of shots.

with the Arrhenius-like temperature dependence which is shown in F4.6. In this regime the thermal activation energy is sufficient for the charge carriers to be activated for taking part in the conduction process. This activated Arrhenius behavior can be expressed by the following equation.[60]

$$R(T) = R_0\, e^{\frac{E_A}{k_B T}} \qquad 4.5$$

Where $R(T)$ is the measured resistance at different temperature T. R_0 is a pre factor, K_B is the Boltzman constant, and E_A is the activation energy barrier. The slope of the fitted line of *ln(R)* versus *1/T* plot helps us calculate E_A for different RGO samples shown in T4.2 which are comparable to the values for graphene based materials reported previously.[60] Arrhenius type of activation energy is the energy equal to the difference between the Fermi energy (E_F) and the energy where the peak of the density of states (DOS) occurs in the energy vs DOS diagram.[61] From the calculation I found that the

activation energy is minimum for the sample with maximum mobility i.e. in sample C. With the deviation of the mobility from its maximum the activation energy in the

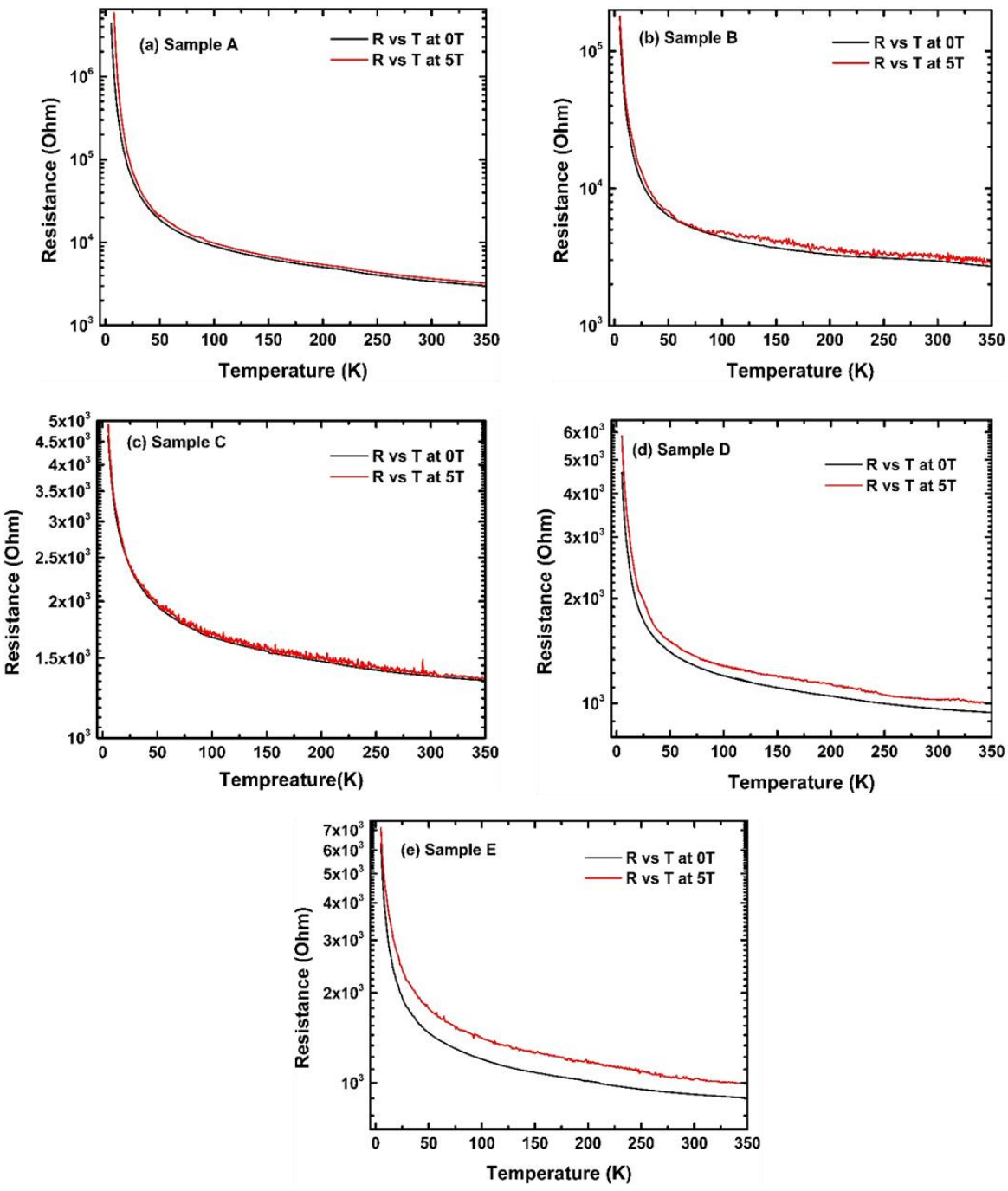

Figure 4.5: Resistance vs temperature data at 0T and 5T magnetic field of (a) sample A, (b) sample B, (c) sample C, (d) sample D, and (e) sample E.

corresponding samples increases which implies that an extra amount of energy is required for the charge carriers to be activated to the nearest mobility edge of the valance/conduction band to function the conduction mechanism.

On the other hand below the temperature of 210K the thermal activation energy is not sufficient to energize a significant amount of carriers to the conduction level. In this case the temperature dependent resistance behavior changes from Arrhenius-like temperature dependence to 2 dimensional variable range hopping (2D-VRH) system. Scientists have proposed different 2D models such as ES 2D-VRH and Mott 2D-VRH in the disordered heterogeneous semiconductors where carrier localization and hopping phenomena play crucial roles in conduction mechanism.[34,62] In a number of temperature dependent resistance studies[63,64,65] on RGO, measured data was only fitted with either one of those two 2D VRH models without making any comment on the other VRH system. However, I considered both models to analyze the resistance as a function of temperature data and observed interesting phenomena. In the Ohmic regime the generalized expression of VRH can be expressed in terms of power law as[66]

$$R(T) = R_0 \, e^{(\frac{T_0}{T})^p} \qquad 4.6$$

Where T_0 is the characteristic temperature, and p is the characteristic exponent. The value of p distinguishes different conduction mechanism i.e. p= ½ and 1/3 corresponds to the ES VRH mechanism and Mott VRH mechanism, respectively. At low temperature region of the temperature dependent resistance measurement in our study, while taking care of both models, I obtained significant information from the fitted data. While fitting the temperature vs resistance data with both models, the value of correlation coefficient (R-square) which signifies the goodness of the fitting were found to be close to 0.99.

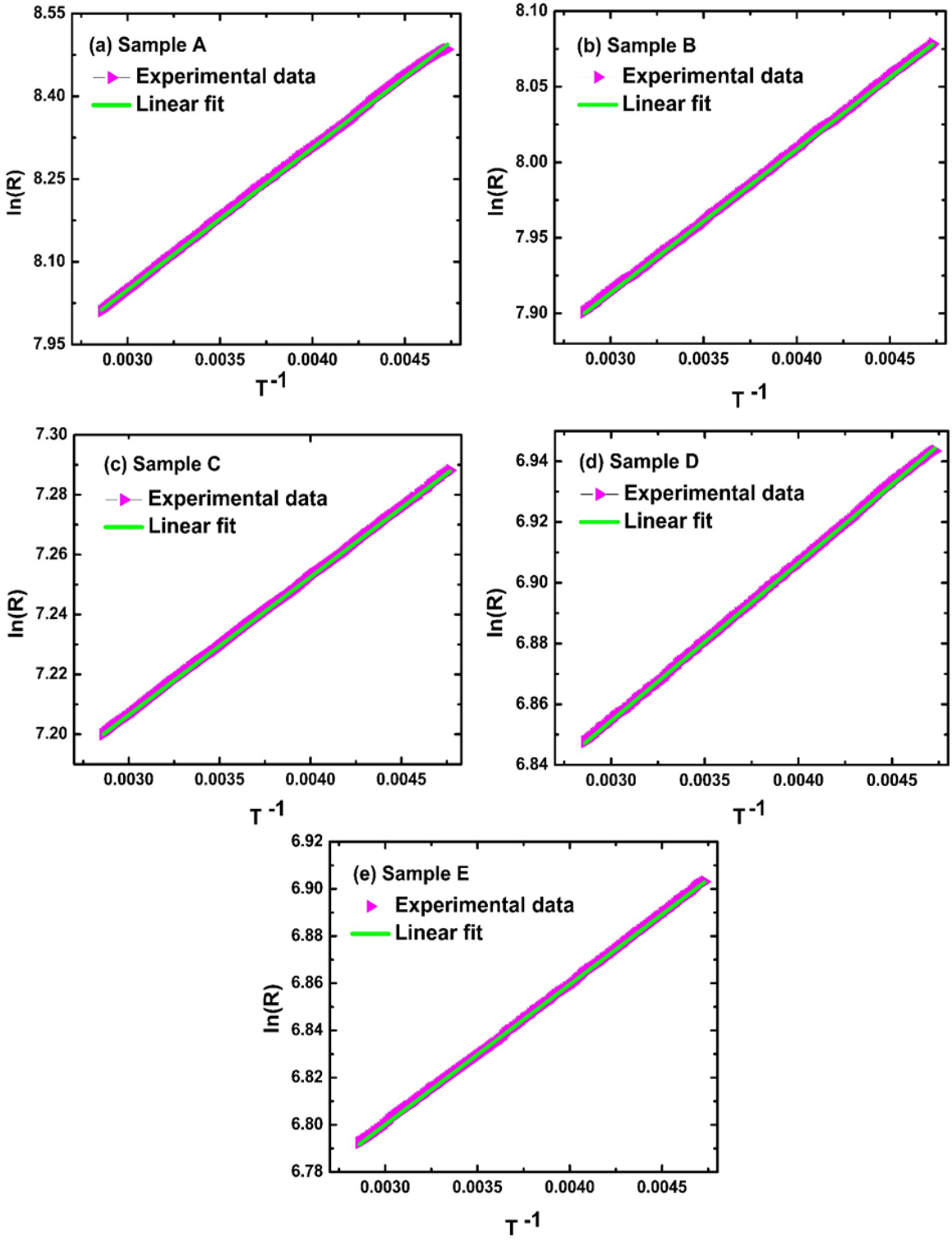

Figure 4.6: *ln(R)* as a function of inverse temperature (T^{-1}) in the temperature range 210K < T < 350K to illustrate the band-gap dominated Arrhenius-like temperature dependence transport mechanism of the representative 5 samples.

With increasing mobility the relationship between temperature and resistance appear closer to the Mott VRH from ES VRH model.

When an electron hops from one electronic state to another neighbor state leaving a hole behind, it needs enough energy to overcome the Columbic interaction between the electron and hole. This barrier energy is known as the Columbic energy gap, E_{CG} which depends on the disorderness of the sample. This phenomena results in a correlation between the measured resistance and temperature that follows the ES VRH model. The characteristic temperature, T_{ES} in this system can be expressed by the following equation.[66]

$$T_0 = T_{ES} = \frac{2.8\, e^2}{4\,\pi\varepsilon\varepsilon_0 k_B \xi} \qquad 4.7$$

Where ε_0 is the permittivity in vacuum, ε is the dielectric constant of the material, and k_B is the Boltzmann constant.

From the slope of equation 4.6, I interpreted the value of the characteristic temperature in this ES VRH model and calculated the localization length using the above equation. The calculated value of the localization lengths for different samples are tabulated in T4.2. As the graphitic domain size obtained from Raman analysis is comparable to the localization length ($L_D \sim \xi$) I can replace k by $1/\xi$ in $E(k) = \hbar v_F k$ to obtain the following equation which allows us to calculate the energy band gap (E_g).[66]

$$E_g = \frac{\hbar v_F}{\xi} \qquad 4.8$$

Where $\hbar$ is the reduced plank's constant, v_F is the graphene Fermi velocity (~10^6 ms^{-1}). The obtained value of energy band gap is tabulated in T4.2.

In VRH models the hopping energy, E_{hop} and the hopping distances, R_{hop} are two significant parameters to interpret the transport properties of the RGO thin film. For ES

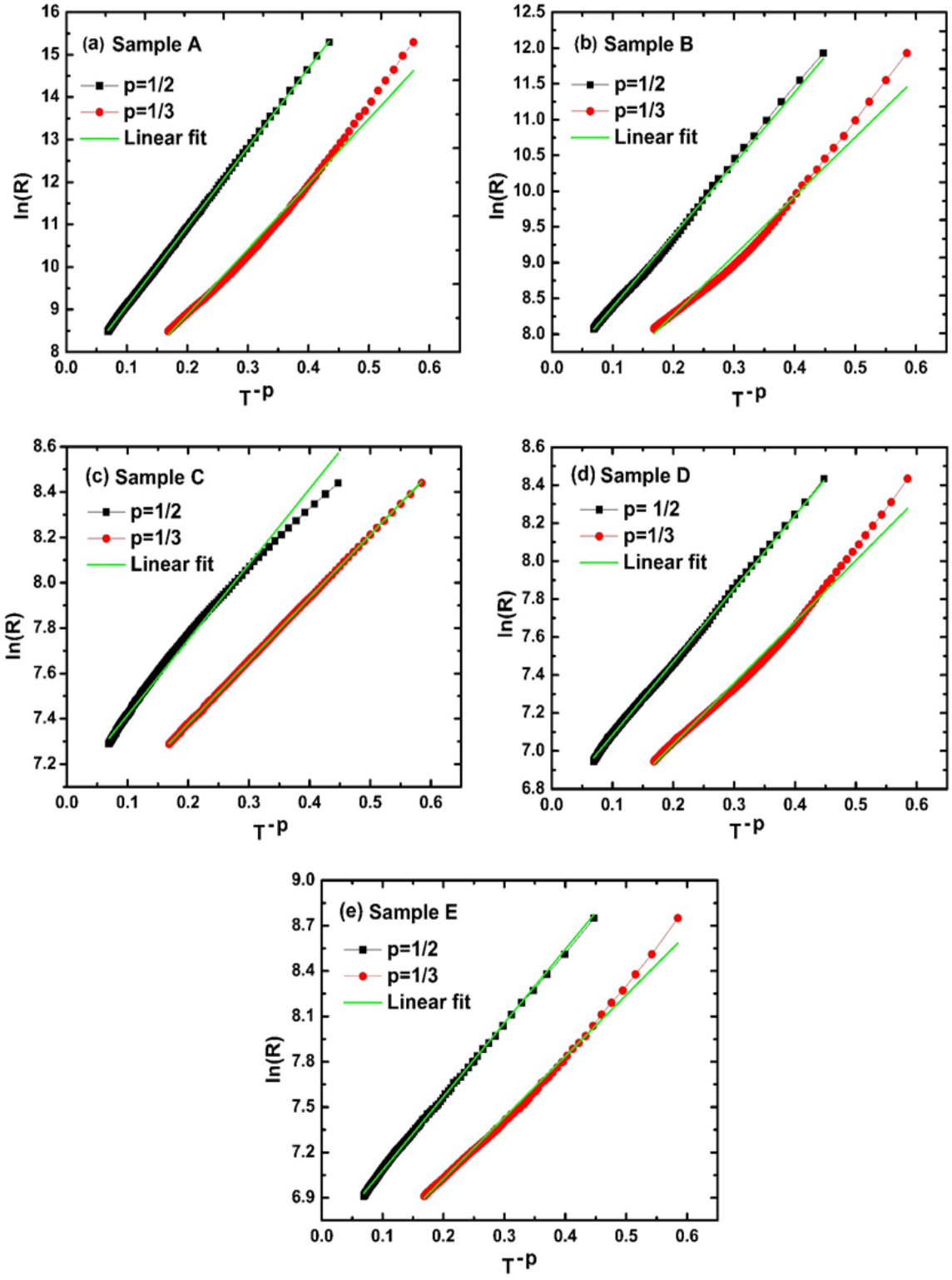

Figure 4.7: Mott VRH and ES VRH region are identified by plotting *ln(R)* as a function of $T^{-1/2}$ and $T^{-1/3}$ in the temperature range 5K < T < 210K in (a) sample A, (b) sample B, (c) sample C, (d) sample D, and (e) sample E.

VRH model these two parameters can be expressed by the following equations and I considered the value of temperature, *T* to be 10K.[67, 68]

$$E_{hop} = \frac{1}{2}\, T_{ES}^{\frac{1}{2}} T^{\frac{1}{2}} \quad 4.9$$

$$R_{hop} = \frac{\xi}{4}\, (\frac{T_{ES}}{T})^{\frac{1}{2}} \quad 4.10$$

In this system the localized charge carriers are responsible for the long range nature of the Coulomb potential which has a significant effect on the charge carrier transport mechanism. This phenomena is instrumental to the vanishing nature of the constant density of localized states near the Fermi level. So the degree of the localization can be anticipated by E_{CG} which is obtained using the following equation-

$$E_{CG} = \frac{T_{ES}}{\beta \sqrt{(4\pi)}} \quad 4.11$$

From the calculated value of the E_{CG} it is evident that the degree of localization increases with the diversion from maximum mobility sample. Lee *et al*.[62] reported that the reduced coulomb energy gap is the outcome of improved screening in the samples. Sample C with minimum E_{CG} implies the less disorderness and strong proximity towards Mott VRH. This fact is also supported by the fitting information where better fitting correlations were obtained with increasing mobility in the samples for Mott VRH model. *D. Joung et al.*[83] also reported that in the less disordered samples it becomes easier for the charge carriers to overcome the E_{CG} which results a constant DOS at E_F. This is an important interpretation of Mott VRH mechanism. So the negligible interactions between the charge carriers in the hopping process changes the exponent in equation 2 from p=1/2 to p=1/3. From the fitting information of *ln(R)* as a function of temperature in F4.7 I have found that the goodness of fitting with Mott VRH model improved with increasing

mobility and decreasing disorderness. Sample C best fitted with the Mott VRH model, whereas the other samples showed a crossover between ES and Mott VRH which refers to the intermediate disorderness in those samples. As all the samples fit well with equation (1) for p=1/3 too, I determined the characteristic temperature, T_M for Mott VRH model. The value of T_M was used to calculate the DOS at E_F, $N(E_F)$ using the following expression.[66]

$$T_0 = T_M = \frac{3}{K_B N(E_F) \xi^2} \quad 4.12$$

Using the Mott VRH model I figured out the evaluation of important hopping parameters such as hopping energy and hopping distance in the as synthesized samples. The following equations were used for the calculation and I tabulated these values in T4.3.[67,68]

$$E_{hop} = \frac{1}{3} T_M^{\frac{2}{3}} T^{\frac{1}{3}} \quad 4.13$$

$$R_{hop} = \frac{\xi}{3} \left(\frac{T_M}{T}\right)^{\frac{1}{3}} \quad 4.14$$

Therefore it is evident that the transport mechanism in high mobility samples is mainly governed by the Mott VRH, while the transport process in the RGO samples comes closer to ES VRH with increasing defect density and disorderness. The impact of this crossover is evident by the decreasing trend of charge carrier mobility in the other samples. The sample quality is also reflected by the hopping energy and hopping distance calculated by following both models. Overall, significant correlation is found between charge carrier Hall mobility, localization length, degree of localization, density of states (DOS) at Fermi level and hopping energy.

Table 4.2 Calculated electrical parameters of the RGO samples.

Sample	Mobility	Localization Length (nm)	E_A (meV)	R_{hopp} (nm)	E_{hopp} (meV)	E_{CG} (meV)	E_g (meV)
A	249	38.4	22.14	56.56	29.46	35	17.2
B	906	133.4	8.46	105	15.803	10	4.94
C	1596	1414	3.98	343	4.856	0.95	0.47
D	612	898	4.48	273.6	6.094	1.5	0.74
E	464	561	5.26	216	7.706	2.4	1.18

Table 4.3 Electrical parameters of sample A, B, C, D and E.

Sample	Carrier concentration	DOS ($cm^{-2}ev^{-1}$)	R_{hopp} (nm)	E_{hopp} (meV)	R_{hop} / ξ
A	$1.72x10^{12}$	6.53×10^{15}	62	169.21	1.618
B	$2.83x10^{12}$	3.45×10^{15}	107	49.2	1.28
C	$4.03x10^{12}$	8.19×10^{14}	606	5.51	0.428
D	$1.61x10^{13}$	1.29×10^{15}	448	7.47	0.4988
E	$1.84x10^{12}$	1.67×10^{15}	351	11.76	0.626

4.4 Magnetoresistance Study

The influence of magnetic field on the temperature dependent electronic property in all the samples was investigated and the plots are represented in F4.5. A magnetic field of 5T was applied parallel to the RGO thin film in the same temperature dependent resistance measurement set up. After reaching the temperature to 5 K, the magnetic field

was applied and a steady sweeping mode of temperature increment was maintained until the system temperature reached to 350 K. The resistance was measured once per 0.5 K temperature increment. The measured resistance versus temperature data in presence of the perpendicular electric field show similar characteristic as the same measurement under zero magnetic field but there was an overall increase of resistance when the field was applied. The difference between these two data plots decreases gradually with the increase in temperature. Hence, at the low temperature region the calculated value of MR is greater than the high temperature region. This positive magneto resistance was obtained using the following formula.[69]

$$MR\ (B) = R(B)/R(0)-1 \qquad 4.15$$

Table 4.4 Percentage of MR at different temperatures in the RGO samples.

Sample	% of MR at 25K	% of MR at 300K	% of MR at 350K
Sample A	26.87	7.5	7.46
Sample B	17.98	7.97	6.67
Sample C	7.15	1.4	0.8
Sample D	13.91	6.22	5.74
Sample E	23.86	12.05	11.78

It has been studied in the earlier research that the VRH mediated in 2D systems show positive MR due to the localization effect.[70] In fact, the weak localization and weak anti-localization simultaneously affect the resistive property in disordered graphene

based materials under the magnetic field. However, the dominance of one onto another can be estimated by the type and amount of obtained MR. From our data it is evident that the weak anti-localization has the dominant effect in the measured MR value at low temperature region. Which means in the occurrence of quantum interference, the localization of the charge carriers is yielded by the destructive interference between the electron wave and the magnetic field. Due to the effect of weak antilocalization, Ortmann *et al.*[27] also observed a positive MR effect in graphene based material. From this study they also found that the weak anti-localization and pseudospin effects become suppressed in the presence of graphene edges and boundaries. Additionally, the long range coulomb scattering potential can be incorporated to interrelate the MR effect in different films. In our experiment the value of the coulomb potential decreases up to sample C and again starts increasing, which has been reflected in the MR measurement. Therefore it is not surprising to observe the value of the positive MR decreases from sample A to sample C, and again increases from sample C to sample E. In multilayer epitaxial graphene Friedman *et al.*[71] suggested that the source of positive MR can be attributed to the inhomogeneity in the sample. The decrease in the MR with the raise in temperature implies Arrhenius effect; more number of electron available in the conduction process which results an increase in the electron wave density. As a result the effect of destructive interferences weaken down. Additionally I cannot originate the weak anti-localization (WAL) for MR effect because usually WAL is a low temperature phenomena when the charge carriers become localized. At the high temperature region I can recall Parish and Littlewood's explanation on non-saturating positive MR in samiconductors which are disordered and strongly inhomogeneous.[72,73] They incorporated a random resistor

network model with four terminals for the inhomogeneous semiconductor to analyze the nonsaturating positive MR effect. Our semiconducting 2D system with crystalline RGO regions fits well to the model which can only produce a transverse magnetoresistance. Because longitudinal MR requires a 3D network. Researchers also followed the quantum route to explain positive MR, but they incorporated gapless material.[74] But I cannot incorporate the quantum route to explain the resultant MR effect in the RGO samples because from the electrical measurements I found distinct bandgap in all the RGO samples.

4.5 Discussion

There are several parameters those contribute to the mobility in the RGO thin films. Among them the localization length, columbic energy gap, disorderness in the film, percolation effects in the tenuously connected films at least in the films grown by a fewer number of shots, and hopping energy all play a crucial role. A good fitting profile of the measured transport data is essential but not sufficient to explain the quality of the thin films. In this situation Raman and XPS investigation provide significant information to support the result obtained from transport property analysis.

I cannot determine any general trend between carrier concentration and mobility in the RGO samples. Because in sample to samples the mobility is limited by a number of scattering mechanisms such as coulomb scattering, resonant impurity scattering, scattering on remote interfacial phonons in Si/SiO_2 substrate, scattering on graphene acoustic phonons etc. at different level of charge carrier density. Hence it is obvious that the obtained carrier mobility in the RGO based devices can only be compared at the same

level of carrier density. This observation complies with other similar graphene based studies.[75]

Muchharala *et al.*[76] reported several application of graphene based materials including optical detectors and modulators having activation energy gap below 100 meV. In all the samples I found the energy barrier well below than 100meV and I can tune this barrier height by tuning the process parameters. Generally in case of a simple energy gap the DOS is expected to increase linearly above and below the gap. From the calculated data it is evident that with broadening the energy gap, the calculated DOS increases which attributes to the good semiconducting feature of the as fabricated thin films. Upon decreasing the mobility with increasing DOS at E_F a strong localized regime is incorporated. In this localized system the Columbic interaction between the states become significant and the amount of E_{CG} increases with stronger localization of the charge carriers.[76] In case of sample A, the DOS at E_F is found to be maximum when E_{CG} is maximum. A decreasing trend in the localization length also refers to stronger localization of the charge carriers. Sample C with maximum charge carrier mobility shows longer localization length which refers to the less disorderness in the sample. In less disordered and more continuous sample the interaction between the charge carriers becomes negligible and the value of E_{CG} is found to be minimum (0.95 meV). As a result it is comparatively easier for the mobile charge carriers to overcome the smaller E_{CG} to generate higher mobility. The stronger localization is also evident by the larger value of E_{CG} in rest of the samples. So, the sample C where the least localization occurred has shown more proximity to Mott VRH model. Whereas with deviation from the growth parameter of sample C, the localization became stronger and the samples displayed

closeness to the ES VRH model. Overall in all the samples I found that the stronger the localization the less the charge carrier mobility. The strong localization of charge carriers also influences the hopping energy and hopping distance. These two parameters increase and decrease respectively with robust localization. It is also worth mentioning that the R_{hop}/ξ ratio is minimum for the sample C with maximum mobility which complies with the increasing trend of T_{Mot} reported by Yildiz *et al*.[77] In a number of previous studies,[78,79,80] it is further noted that the measured characteristic parameters for both VRH models are in the same order of magnitude. Our measured values also completely follow those observations. For temperature greater than 210 K the localization interaction might quench and be subdued by Arrhenius activated mechanism of charge carrier transportation.

In sample to sample with variation in number of shots, the value of T_0 varies from 8K to 350K which implies that the number of shots has a large influence on the electrical transport property of the as grown thin films. This interpretation is further supported by the other spectroscopic information. In this experiment initially I used the transferred graphene as base layer which inherently is discontinuous, and therefore it showed unmeasurable resistance. The deposition of GO plume on this base layer acts as filler to those discontinuous zones. In sample A the fewer number of laser shots for the oncoming plume means it cannot bridge all the disjointed sp^2 regions. With increasing number of shots better continuity is supposed to be achieved and thus the mobility should raise. But experimentally it is found that the charge carrier Hall mobility increases up to the region of 5000 shots and then starts decreasing which is depicted in F4.4. Because the pulse laser deposition of GO on the substrate also incorporates defects, impurities, and zone

boundary along with sp^3 clusters are evident by the increment of the *D* band in Raman spectra analysis. The deposition is done at high temperature (700C). Increasing number of shots requires more time to complete the deposition process. Therefore loss of C atoms from the graphene basal plane might also take place. Furthermore in the presence of different functional groups the GO itself is defective and overall the I_D/I_G ratio increases with increasing number of shots. Hence a tradeoff between the number of laser shots and defect density is required to achieve the maximum charge carrier Hall mobility which is termed as a "suitable zone" in this experimental analysis. At this "suitable zone" a considerable continuity in the thin film is achieved at a moderate defect density. Beyond this zone the defect density increases and the I_{2D}/I_G ratio as well as the L_D decrease significantly which causes the decline in mobility. These results are tabulated in T4.1. From the electrical transport property characterization and Raman spectroscopy it is evident that the maximum homogeneity was achieved in sample C which showed the smallest MR effect. On the other hand, deviation from the homogeneity results an increment in the MR effect which are evident in the rest of the samples.

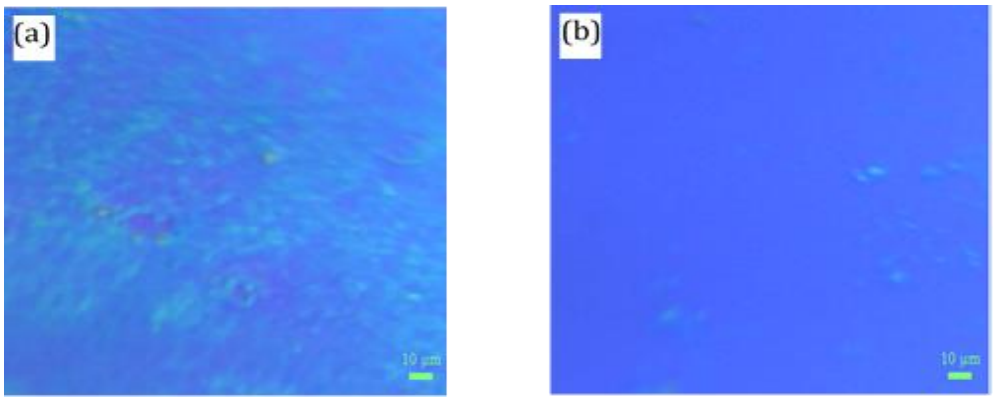

Figure 4.8: Magnified view of (a) sample A (300 shots), and (b) sample C (5000 shots).

CHAPTER 5: CONCLUSIONS

RGO thin films on SiO_2/Si substrates have been fabricated using pulsed laser deposition technique. Improved electronic properties, in particular large charge carrier mobility, have been achieved in RGO thin films through introducing a seed layer of graphene and varying growth parameters of the PLD process. The domain size of sp^2 clusters play an important role to determine the charge carrier mobility. In the temperature dependent resistance measurement, I investigated a crossover phenomenon from ES VRH to Mott VRH with process parameters and obtained estimates of the Coulomb gap as a function of defect density acquired by Raman analysis. The variation in Arrhenius gap in sample to sample also accorded with other electrical parameters. The interesting positive MR effect at low temperatures as well as in room temperature opens up the feasibility of PLD grown large area RGO thin film to be used in magneto sensor device application. In this experimental work I have also been able to identify the suitable zone where the charge carrier hall mobility is maximum. Overall this study will help to carry on the investigation of the electronic as well as magnetic properties in large area RGO samples for future device application.

REFERENCES

[1] A. Buchsteiner, A. Lerf, and J. Pieper, J. Phys. Chem. B **110,** 22328 (2006).

[2] M. D. Stoller, S. Park, Y. Zhu, J. An, and R. S. Ruoff, Nano Lett. **8,** 3498 (2008).

[3] C. Lee, X. Wei, J. W. Kysar, and J. Hone, Science. **321,** 385 (2008).

[4] K.I. Bolotin, K.J. Sikes, Z. Jiang, M. Klima, G. Fudenberg, J. Hone, P. Kim, and H. L. Stormer, Solid State Commun. **146,** 351 (2008).

[5] A. A. Balandin, S. Ghosh, W. Bao, I. Calizo, D. Teweldebrhan, F. Miao, and C. N. Lau, Nano Lett. **8,** 902 (2008).

[6] J. I. Paredes, S. Villar-Rodil, P. Solis-Fernandez, A. Martinez-Alonso, and J. M. D. Tascon, Langmuir. **25,** 5957 (2009).

[7] I. Jung, M. Vaupel, M. Pelton, R. Piner, D. A. Dikin, S. Stankovich, J. An, and R. S. Rouff, J. Phys. Chem. C **112,** 8499 (2008).

[8] O. Akhavan, Carbon **48,** 509 (2010).

[9] G. Eda, and M. Chhowalla, Nano Lett. **9,** 814 (2009).

[10] H. Y. He, J. Klinowski, M. Forster, and A. Lerf, Chem. Phys Lett. **287,** 53 (1998).

[11] A. Lerf, H. He, M. Forster, & J. Klinowski, J. Phys. Chem. B **102,** 4477 (1998).

[12] Cai, W. et al. Synthesis and solid-state NMR structural characterization of 13C-labeled graphite oxide. Science **321,** 1815 (2008).

[13] W. Gao, L. B. Alemany, L. Ci, and P. M. Ajayan, Nature Chem. **1,** 403 (2009).

[14] A. Bagri, C. Mattevi, M. Acik, Y. J. Chabal, M. Chhowalla, and V B. Shenoy, Nature Chem. **2,** 581 (2010).

[15] X. Wu, M. Sprinkle, X. Li, F. Ming, C. Berger, and W. A. de Heer, Phys Rev Lett. **101**, 026801 (2008).

[16] R. D. Daniel, P. Sungjin, W. B. Christopher, and S. R. Rodney, Chem Soc Rev. **39**, 228 (2010).

[17] O. Frank, C. Alessandro, M. Gilles, and R. Stephan, Europhys. Let. 94(4), 1 (2011).

[18] B. Muchharla, T. N. Narayanan, K. Balakrishnan, P. M. Ajayan, and S. Talapatra, 2D Mater. **1**, 011008 (2014).

[19] S. W. Wang, H. E. Lin, H. D. Lin, K.Y. Chen, K. H. Tu, and C. W. Chen, Nanotech. **22**, 33570-1 (2011).

[20] N. W. Ashcroft, and N.D. Mermin, Solid State Physics. New York, 1976.

[21] K . Gopinadhan, Y.J. Shin, I. Yudhistira, J. Niu, and H. Yang, Phys. Rev. B. **88**, 195429 (2013).

[22] P.A. Bobbert, T. D. Nguyen, FWaV. Oost, B. Koopmans, and M.Wohlgenannt, Phys. Rev. Lett. **99**, 21680-1 (2007).

[23] H. Paul, and D. Mohanta, Appl Phys A. **103**, 395 (2011).

[24] N. A. Kotov, I. De´ka´ny, and J. H. Fendler, Adv. Mater. **8(8)**, 637 (1996).

[25] M. J. Fernandez-Merino, L. Guardia, J. I. Paredes, S. Villar-Rodil, P. Solis-Fernandez, and A. Martinez-Alonso, J. Phys. Chem. C **114(14)**, 6426 (2010).

[26] Y. Zhu, S. Murali, M. D. Stoller, A. Velamakanni, R. D. Piner, and R. S. Ruoff, Carbon. **48(7)**, 2118 (2010).

[27] Y. Zhang, L. Guo, S. Wei, Y. He, H. Xia, and Q. Chen, Nanotoday **5(1)**, 15 (2010).

[28] H. Wang, J. T. Robinson, X. Li, and H. Dai, J. Am. Chem. Soc. **131(29)**, 9910 (2009).

[29] G. Eda, G. Fanchini, and M. Chhowalla, Nat. Nanotechnol **3(5)**, 270 (2008).

[30] H. C. Schniepp, J.L. Li, M. J. McAllister, H. Sai, M. Herrera-Alonso, and D. H. Adamson, J.Phys. Chem. B **110(17)**, 8535 (2006).

[31] S. Stankovich, D.A. Dikin, R. D. Piner, K. A. Kohlhaas, A. Kleinhammes, and Y. Jia, Carbon **45(7)**, 1558 (2007).

[32] V. C. Tung, M. J. Allen, Y. Yang, R. B. Kaner, Nat. Nanotech. **4**, 25 (2009).

[33] W. Jianwei, S. Budhi, P. Jin-Hyung, R. Servin, L. In-yeal, M. Sunglyul, J. Han-Ik, L. Cheol-Ho, and K. Gil-Ho, Sensors and Actuators B: Chem. 194, 296 (2014).

[34] B. I. Shklovskii, A. L. Efros, Electronic Properties of Doped Semiconductors. Springer-Verlag: Berlin, 202 (1984).

[35] A. Miller, and E. Abrahams, Phys. Rev. **120**, 745 (1960).

[36] A. Egea-Guillen, M. Ortuno, and R. Garcia-Molina, Phys. Rev. B. **50**, 12520 (1994).

[37] A. L. Efros, B. I. Shklovskii, J. Phys. C: Solid State Phys. **8**, 49 (1975).

[38] R. Eason, Pulsed Laser Deposition of Thin Films: Applications-Led Growth of Functional materials, John Wiley and Sons, Inc., Publication, 2007.

[39] J. R. Ferraro, K. Nakamoto, and C. W. Brown, Introductory Raman Spectroscopy, Elsevier Inc., 2003.

[40] B. E. Warren, X-Ray Diffraction, Dover Publications; Reprint edition, 2012.

[41] J. Clarke and A. I. Braginski, A Review of: The SQUID Handbook: Fundamentals and Technology of SQUIDS and SQUID Systems, Taylor and Francis, 2006.

[42] J. Hall, J. Allanson, K. Gripp , and A. Slavotinek, Handbook of Physical Measurements, Oxford Handbook Series, 2006.

[43] A. C. Ferrari, J. C. Meyer, V. Scardaci, C. Casiraghi, M. Lazzeri, F. Mauri, S. Piscanec, D. Jiang, K. S. Novoselov, S. Roth, and A. K. Geim, Phys. Rev. Lett. **97**, 18740-1 (2006).

[44] M. A. Pimenta, G. Dresselhaus, M. S. Dresselhaus, L. G. Cancado, A. Jorio, and R. Saito, Phys. Chem. Chem. Phys. **9**, 1276 (2007).

[45] B. Krauss, T. Lohmann, D. H. Chae, M. Haluska, K. V. Klitzing, and J. H.Smet, Phys. Rev. B. **79**, 165428-1 (2009).

[46] L. G. Cançado, A. Jorio, E. H. M. Ferreira, F. Stavale, C. A. Achete, and R. B. Capaz, Nano Lett. **11**, 3190 (2011).

[47] C. Y. Su, Y. Xu, W. Zhang, J. Zhao, X. Tang, C. H. Tsai, and L. J. Li , Chem. of Mater. **21**, 5674 (2009).

[48] D. Zhan, Z. Ni, W. Chen, L. Sun, Z. Luo, L. Lai, Ting Yu, A. T. S. Wee, and Z. Shen, Carbon **49**, 1362 (2011).

[49] S. Some, Y. Kim, Y. Yoon, H. J. Yoo, S. Lee, Y. Park, and H. Lee, Sci. Rep. **3**, 1929-1 (2013).

[50] D. C. Marcano, D. Kosynkin, M. J. Berlin, A. Sinitskii, Z. Sun, A. Slesarev, L. B. Alemany, W. Lu, and J. M. Tour, ACS Nano. **4**, 4806 (2010).

[51] H. H. Seung, Thermal reduction of graphene oxide, physics and applications of graphene experiments. Dr.Sergey Mikhailov In Tech. 2011.

[52] W. L. Bragg, and W. H. Bragg, The Crystalline State. G. Bell & Sons Ltd, New York: 1934.

[53] M. McKeehan, and B. E. Warren, J. Appl. Phys. **24**, 52 (1953).

[54] H. M. Ju, S. H. Huh, S. H. Choi, and H. L. Lee, Mater. Lett. **64**, 357 (2010).

[55] M. Rein, N. Richter, K. Parvez, X. Feng, H. Sachdev, M. Kläui, and K. Müllen, ACS Nano. **9**, 1360 (2015).

[56] S. Pei, and H. M. Cheng, Carbon. **50**, 3210-3228 (2011).

[57] H. Xu, Z. Zhang, R. Shi, H. Liu, Z. Wang, S. Wang, and L. M. Peng, Sci. Rep. **3**, 1207-1 (2013).

[58] Y. W. Tan, Y. Zhang, H. L. Stormer, and P. Kim, Eur. Phys. J. Special Top. **148**, 15 (2007).

[59] S. V. Kravchenko, M. P. Sarachik, Rep Prog Phys. **67**, 1−44 (2004).

[60] B. Muchharla, A. Pathak, Z. Liu, L. Song, T. Jayasekera, S. Kar, R. Vajtai, L. Balicas, P. M. Ajayan, S. Talapatra, and N. Ali, Nano Lett. **13**, 3476 (2013).

[61] M. Pollak and M. Ortuno, Electron-Electron interactions in Disordered Systems, edited by A. L. Efros and M. Pollak, North-Holland, Amsterdam, 1985.

[62] N. F. Mott, and E. A. Davis, Electronic Processes in Non-Crystalline Materials. Oxford: Clarendon press, 1971.

[63] G. Eda, C. Mattevi, H. Yamaguchi, H. Kim, and M. Chhowalla, J. Phys. Chem. C. **113**, 15768 (2009).

[64] C. G. Navarro , R. T. Weitz , A. M. Bittner, M. Scolari , A. Mews, M. Burghard, and K. Kern, Nano Lett. **7**, 3499 (2007).

[65] R. McIntosh, M. A. Mamo, B. Jamieson, S. Roy, and S. Bhattacharyya, Europhys. Lett. **97**, 38001-1 (2012).

[66] D. Joung, S. I. Khondaker Efros-Shklovskii, Phys. Rev. B **86**, 235423-1 (2012).

[67] S. J. Lee, J. B. Ketterson, and N. Trivedi, Phys. Rev. B **46(19)**, 12695 (1992).

[68] R. Rosenbaum, Phys. Rev. B **44**, 3599 (1991).

[69] T. Ciuk, J. Krupka, C. Jastrzebski, J. Judek, W. Strupinski, S. Butun, E. Ozbay and M. Zdrojek, J. of Mat. Sci. and Eng. A. **2 (7),** 489 (2012).

[70] C. M. Wang, and X. L. Lei, Phys. Rev. B **86**, 035442 (2012).

[71] A. L. Friedman, J. L. Tedesco, P. M. Campbell, J. C. Culbertson, E. Aifer, F. K. Perkins, Nano Lett. **10(10)**, 3962 (2010).

[72] M. M. Parish, P. B. Littlewood, Nature **426**, 162 (2003).

[73] J. Hu, and T. F. Rosenbaum, Nature Mat. **7**, 697 (2008).

[74] A. A. Abrikosov, Phys. Rev. B **58**, 2788 (1998).

[75] S. Viera, and B. K. Alan, Graphene Properties, Preparation, Characterization and Devices. Wood Head Publishing Inc, 2014.

[76] C. J. Adkins, J. Phys. Condens. Matt. **1(7)**, 1253 (1989).

[77] A. Yildiz, S. B. Lisesivdin, M. Kasap, and D. Mardare, J. Non-Crystall Sol. **354(45)**, 4944 (2008).

[78] A. Dey, S. De, A. De, and S. K. De, Nanotechnology **15**, 1277 (2004).

[79] R. K. Roy, S. Gupta, and A. K. Pal, Thin Solid Films **483**, 287 (2005).

[80] A. K. Hassan, N. B. Chaure, A. K. Ray, A. V. Nabok, and S. Habesch, J. Phys. D **36**, 1120 (2003).